3D Full-Field Quantification of Cell-Induced Large Deformations in Fibrillar Biomaterials by combining Non-Rigid Image Registration with Label-free Second Harmonic Generation

Alvaro Jorge-Peñas[ǂ1], Hannelore Bové[ǂ2], Kathleen Sanen[2], Marie-Mo Vaeyens[1], Christian Steuwe[3], Maarten Roeffaers[3], Marcel Ameloot[2ǂ], Hans Van Oosterwyck[1,4ǂ*]*

[1] Department of Mechanical Engineering, KU Leuven, Celestijnenlaan 300C – box 2419, Leuven, Belgium

[2] Biomedical Research Institute, Hasselt University, Agoralaan Building C, 3590 Diepenbeek, Belgium

[3] Centre for Surface Chemistry and Catalysis, KU Leuven, Celestijnenlaan 200F, Leuven, Belgium

[4] Prometheus, div. Skeletal Tissue Engineering, KU Leuven, Leuven, Belgium

ǂ These authors contributed equally to this work

* hans.vanoosterwyck@kuleuven.be and marcel.ameloot@uhasselt.be

KEYWORDS: Large deformation; fibrillar hydrogel; Second Harmonic Generation; traction force microscopy; non-rigid image registration.

ABSTRACT

To advance our current understanding of cell-matrix mechanics and its importance for biomaterials development, advanced three-dimensional (3D) measurement techniques are necessary. Cell-induced deformations of the surrounding matrix are commonly derived from the displacement of embedded fiducial markers, as part of traction force microscopy (TFM) procedures. However, these fluorescent markers may alter the mechanical properties of the matrix or can be taken up by the embedded cells, and therefore influence cellular behavior and fate. In addition, the currently developed methods for calculating cell-induced deformations are generally limited to relatively small deformations, with displacement magnitudes and strains typically of the order of a few microns and less than 10% respectively. Yet, large, complex deformation fields can be expected from cells exerting tractions in fibrillar biomaterials, like collagen. To circumvent these hurdles, we present a technique for the 3D full-field quantification of large cell-generated deformations in collagen, without the need of fiducial markers. We applied non-rigid, Free Form Deformation (FFD)-based image registration to compute full-field displacements induced by MRC-5 human lung fibroblasts in a collagen type I hydrogel by solely relying on second harmonic generation (SHG) from the collagen fibrils. By executing comparative experiments, we show that comparable displacement fields can be derived from both fibrils and fluorescent beads. SHG-based fibril imaging can circumvent all described disadvantages of using fiducial markers. This approach allows measuring 3D full-field deformations under large displacement (of the order of 10 μm) and strain regimes (up to 40%). As such, it holds great promise for the study of large cell-induced deformations as an inherent component of cell-biomaterial interactions and cell-mediated biomaterial remodeling.

1. INTRODUCTION

During the last decade studies have shown significant differences in morphology and behavior of cells when embedded in three-dimensional (3D) environments compared to seeding them onto two-dimensional (2D) substrates [1–3]. A critical component is the extracellular matrix (ECM), which provides biophysical and biochemical cues to resident cells via cell-matrix interactions. It is generally accepted that along with the chemical signals, mechanical properties and cues play a crucial role during many physiological and pathological processes including development, growth, regeneration and disease states like cancer metastasis [4–6]. Hence, the quantification of cell-matrix mechanical interactions within 3D environments is extremely important for enhancing our current understanding of these processes, as well as for developing biomaterials that exploit the role of these mechanical interactions in controlling cell fate [7–10].

Cell-matrix mechanical interactions are most commonly investigated using traction force microscopy (TFM). In TFM, tractions are computed from measured cell-induced matrix displacements [11]. TFM involves solving an inverse problem, which requires a mathematical (computational) approach that, apart from displacement data, requires information on ECM mechanical (elastic) properties. This method was initially developed for cells on 2D planar substrates [12–14] that have a number of practical advantages compared to 3D, such as the use of non-degradable substrates with linear elastic properties that are stable over time, compatibility with high resolution imaging and the availability of well-established methods to recover high resolution displacement and traction fields. More recently, TFM has been extended to the recovery of 3D force fields exerted by cells encapsulated in linear elastic, non-fibrillar [15] and non-linear elastic, fibrillar ECMs [16]. Especially for 3D setups traction recovery is not trivial, neither experimentally nor computationally, among others because of the continuous remodeling of the ECM by cells, which could alter the local constitutive behavior of the matrix and therefore

compromise the validity of recovered tractions [17]. On the other hand, cell-induced matrix displacements already provide quantitative information on the magnitude, orientation and distribution of cell-matrix mechanical interactions [17], avoiding the tedious task of characterizing ECM mechanical properties and the computational complexity of solving for the unknown forces.

To calculate cell-induced matrix displacements, fluorescent beads are typically embedded into the extracellular matrix to act as fiducial markers. This approach allows computing the displacements by well-established particle tracking algorithms [15,18] and other algorithms based on local grey scale distribution such as digital image/volume correlation, also known as particle image velocimetry (PIV) [19]. Still, the use of external markers brings about several drawbacks: fluorescent beads could alter the matrix mechanical properties and cells could detach and engulf the beads from the ECM, which could affect cell behavior and introduce errors caused by bead motion. Moreover, the accuracy and spatial resolution of the computed displacements strongly depends on the bead density used in the experiments. It must be high enough to capture cell-induced complex matrix deformations in order to avoid the loss of local, high-frequency spatial information [20,21]. Recently, PIV has been used to quantify cell-induced displacements in 3D fibrillar ECMs by directly imaging (by means of confocal reflectance microscopy) the fibrils without the need of fiducial markers [16,22]. However, the quality of the displacements computed from fibril image data has not been compared yet to displacements computed from fluorescent bead image data, which can be considered the reference method. Moreover, while PIV has been proved suitable for quantifying displacements under relatively small strain (less than 10%) regimes [22], alternative algorithms based on iterative image warping schemes such as fast iterative digital volume correlation (FIDVC) [23] or non-rigid free form deformation (FFD) based image registration [24] should be considered to deal with large strains. These algorithms allow capturing large material deformations while providing a significant increase in the spatial resolution of

the computed displacements by combining a coarse-to-fine approach with an iterative image warping process.

In this study, we demonstrate that FFD-based image registration, combined with label-free, Second Harmonic Generation (SHG) imaging, enables to accurately calculate cell-induced, full field displacements in fibrillar collagen under large deformations (defined here as strain magnitudes larger than 10%). The SHG-signal of collagen type I fibrils has the advantage of yielding high contrast and submicron resolution images in a non-invasive, label-free manner [25,26], making the use of fluorescent beads for displacement field calculations superfluous. In order to assess the quality of the displacements computed from SHG imaging, they will be compared to the displacements obtained from a high density of fluorescent beads attached to the collagen fibrils, which act as control.

2. MATERIALS AND METHODS

2.1. Materials and Products

All chemicals were purchased from Sigma-Aldrich (Belgium) unless stated otherwise.

2.2. Experimental Methods

Cell Culture

Human fetal lung fibroblasts (MRC-5 cell line, ATCC CCL-171, LGC Standards, France) were cultured in 75-cm² flasks in Minimum Essential Medium (MEM, Life Technologies, Belgium) supplemented with 10% fetal bovine serum (FBS, Biochrom AG, Germany), 100 U/mL penicillin, and 100 µg/mL streptomycin at 37°C, 5% CO2 and 95% humidity. At 80-90% confluency cells were routinely sub-cultured using trypsin-EDTA to detach cells. Cells for traction force experiments were seeded on Ibidi µ-slide 8 well (Ibidi GmbH, Germany) plates at a density of 15,000 cells/well and incubated overnight to allow for cell adherence. After washing three times with phosphate buffered saline (PBS), cells were treated for 45 minutes with 12.5 µM CellTracker™ Green CMFDA (Life technologies, Belgium) in serum free cell culture medium. After exposure, cells were washed three times with PBS, detached and mixed with collagen solution before polymerization at a concentration of 15,000 cells/mL.

Synthesis of Collagen Type I Gels with high density of attached beads

Cell-seeded collagen type I hydrogels containing a high density of fluorescent beads were prepared according to a method described previously [16] with some modifications. Briefly, hydrogels were prepared on ice by mixing 8 volumes of collagen consisting of rat tail collagen (collagen type I, 10.31 mg/mL, Corning, The Netherlands) and bovine skin collagen (collagen type I, 5.9 mg/mL, Nutragen,

Advanced Biomatrix, Germany) in complete MEM at a ratio of 1:2 and a final concentration of 2.4 or 4.0 mg/mL diluted with appropriate amount of 10x MEM. Next, 10% (vol/vol) sodium bicarbonate (23 mg/mL) containing 1.0 mg/mL or 1.5 mg/mL fluorescent polystyrene beads (0.2 µm or 1 µm diameter respectively, carboxylated, ex/em 580/605, Invitrogen, Belgium) was added. The pH of the mixture was neutralized using 1 M sodium hydroxide, after which 1 volume of cells were embedded as described in the previous section. The resulting mixture was cast in Ibidi µ-slide 8 well plates (Ibidi GmbH, Germany) at 300 µL/well. The gels were polymerized for 15 minutes at 37°C and subsequently immersed with complete MEM after which they were allowed to set for 18 hours before the start of the displacement experiments.

The spatial resolution of the matrix displacement field directly depends on the density of the sampling points used to capture matrix deformations. In fibrillar biopolymers, the achievable spatial resolution would be mainly limited by the density of the fibrillar network, where fibrils naturally act as the sampling locations of local deformations, while embedded beads must be attached to the fibrils to correctly reflect matrix displacements. Hence, to perform a fair comparison between bead-based and fibril-based matrix displacements, the density of the attached beads must be high enough to comply with Nyquist sampling theorem and act as fiducial markers of the fibrils deformations. To match the displacement sampling between both bead-based and fibril-based images, the bead density was increased. At the same time the bead diameter was lowered from 1 to 0.2 µm in order to keep the total mass of beads in the collagen hydrogel reasonable. Distances between the attached fluorescent beads of the different hydrogel-bead formulations (0.2 μm vs. 1 μm fluorescent beads) were determined using the Nearest Neighbor Distances Calculation plugin of the image processing package Fiji (ImageJ v1.47, Open source software, http://fiji.sc/Fiji). These nearest neighbor distances were plotted against their probability density in histograms using MATLAB (The MathWorks Inc, Natick, MA USA). A Gaussian was fitted to the data. The increase in the bead density resulted in a decreased mean bead-bead distance

from 8.4 to 4.8 µm (Supplementary Figure S1), correlating to a two-fold enhancement of the sampling frequency.

Image Acquisition

Three-dimensional image stacks were acquired using a Zeiss LSM510 META NLO scan head mounted on an inverted laser scanning microscope (Zeiss Axiovert 200M, Zeiss, Germany) and a LD C-Apochromat 40x/1.1 W Korr UV-Vis-IR water immersion objective (Zeiss). The microscope is equipped with a motorized, programmable stage placed on a vibration isolation table in an air-conditioned room kept at a constant temperature of 22°C. Cells were kept at 37°C and 5% CO_2 during the displacement experiments by means of a stage incubator (Tempcontrol 37-2 digital, PeCon, Erbach, Germany).

Label-free SHG imaging of the hydrogels was performed using a femtosecond pulsed laser (MaiTai DeepSee, Spectra-Physics, USA) tuned to a central wavelength of 810 nm as excitation source. The beam was reflected by a short-pass 650 nm dichroic beam splitter and focused onto the sample with an average excitation power of approximately 5 mW on the stage. The SHG signals from the collagen fibrils were epi-collected, discriminated from the autofluorescence of the embedded cells with a 442 nm dichroic beam splitter and transmitted through a 5 nm wide band pass filter with a central wavelength of 405 nm. An analogue photomultiplier tube (Zeiss) was employed for detection in non-descanned mode.

For imaging the CellTracker™-labeled cells inside the hydrogels, a 30 mW air-cooled Argon ion laser (LASOS Lasertechnik GmbH, Germany) emitting at 488 nm (~ 3 µW maximum radiant power at the sample) was employed. A band-pass filter 500 – 530 nm was used for filtering the emission signal. For imaging the fluorescent beads attached to the collagen fibrils, excitation at 543 nm (~ 3 µW maximum radiant power at the sample) was performed by using a 5 mW Helium Neon laser (LASOS Lasertechnik

GmbH). A band-pass filter 565 – 615 nm was used for filtering the emission signal. A fixed pinhole size of 160 μm was used.

Sham Experiments

Three different sham experiments were conducted to rule out or compensate for displacements not related to cellular activity.

First, bead attachment to the fibrils was verified to avoid erroneous displacements caused by the motion of advected and/or diffusing beads. Image series of 50 frames of control acellular hydrogels were acquired. The resulting 1024x1024 images with a pixel size of 0.22 x 0.22 μm^2 were recorded using a pixel dwell times of 1.6 μs. Temporal and spatio-temporal image correlation spectroscopy (TICS and STICS) analyses were performed using custom written MATLAB routines, which have been published previously by the Wiseman Research Group of McGill University [27,28]. Brief explanation of the image correlation spectroscopy analyses can be found in Supplementary Information (Note 1).

Second, time-lapses of control acellular hydrogels were recorded and analyzed to detect the existence of spurious displacements. Over time, z-stacks of fibrils and beads were acquired at the top, middle and bottom part of different hydrogels (total hydrogel height of ~1.5 mm, 15 minutes z-stack acquisition time). Then, for each time point the displacements with respect to the last time point (0 s time interval between z-stacks, 2 h total acquisition time) were computed following the same image processing steps as for the real experiments with cells (see section 2.3). To assess any dependency on experimental setup, protocol or personal handling, the existence of spurious displacements was analyzed for two sets of 3 control hydrogels prepared independently by two different persons and imaged on two different setups, with one setup being the acquisition system used for all other experiments (see section 2.2

'image acquisition'), and the other one being an upright microscope (BX61WI Olympus, Tokyo, Japan) with motorized focusing and a 25x/1.05 water immersion objective.

Third, to rule out any errors induced by the method used to compute the displacements (see section 2.3), 3D synthetic image data of hydrogel volumes containing embedded fluorescent beads as acquired by an optical microscope were generated and analyzed by means of a previously developed TFM simulator [29]. Briefly, this simulator generates ground truth displacements (for known tractions that serve as input) and corresponding microscope images of fluorescent beads in non-deformed and deformed hydrogel configurations, taking into account 'non-ideal' microscope aspects, such as the microscope's point spread function, camera resolution and various sources of noise. By comparing the displacements computed from the synthetic microscope data to the ground truth displacements, errors related to image registration can be assessed. In order to simulate our sham experiments, images were generated for zero tractions, meaning that recovered displacements should also be zero (or corresponding to simulated noise levels), and the parameters of the simulated hydrogel and imaging system were selected to mimic our experimental setup. More specifically, the images of the hydrogel were generated using a model for the point spread function of a laser scanning confocal microscope with a 1.1 NA water immersion objective lens, providing a final voxel size of 0.44 x 0.44 x 0.3 μm^3. The hydrogel contained 0.2 µm fluorescent beads (emission wavelength 605 nm) and its refractive index was set to 1.43. For each simulated time point, the generated z-stacks were corrupted with new realizations of Gaussian and Poisson noise.

Assays for Cell-induced Deformations

A 173 x 173 x 45 μm^3 volume was imaged on average around each cell, including ~7 μm of fibrils/fluorescent beads above and below the cell body. The z-stacks were acquired sufficiently distant from top and bottom of the hydrogel and comprised an average of 41 images with a voxel size of 0.34 x

0.34 x 1 μm^3 recorded using a pixel dwell time of 6.4 μs. After imaging the volume under cellular tractions, the embedded cells were treated with 25 μM cytochalasin B and then reimaged every ~8 minutes for 1 h during cellular relaxation, until the force-free relaxed state of the gel was obtained. The acquired z-stacks were processed as described in section 2.3.

2.3. Computational Methods

Pre-Processing of Acquired Images

Prior to the calculation of the displacements, raw image data were enhanced by a two-step process consisting of a noise filtering step followed by a contrast stretching operation to highlight the structures of interest - beads, fibrils or cells - from the image background. More specific, fibril and cell images were processed by penalized least squares-based denoising [30] and bead images were filtered by a difference of Gaussians operator to simultaneously boost blob-like structures and to reduce noise.

Image Registration for Displacement Field Calculation

The calculation of the displacement fields was split into two different registration processes: a rigid registration where the acquired images were globally aligned to correct for the translational shifts of the microscope stage, followed by a non-rigid registration where the local displacements induced by cellular forces were estimated.

In particular, to correct for stage drift while assuring temporal consistency for time lapse acquisitions, we have performed rigid registration of the images on consecutive time points and then expressed the position of the registered images in a global frame of reference. As for the non-rigid registration, we have made use of a B-spline-based Free Form Deformation approach [24]. Briefly, in FFD-based image registration, the transformation model that warps the image of the stressed state (i.e. hydrogel loaded

by cellular tractions) is given by a multivariate B-spline function. The algorithm overlays the image of the relaxed state (i.e. after adding cytochalasin B) with a regular mesh, and then defines the mesh nodes as the control points of the B-spline curves. Subsequently, the position of these control points is tuned iteratively during the optimization process warping the image of the stressed matrix until it matches the one of the relaxed condition, providing as output a full displacement field, *i.e.* at each voxel of the registered images. Although the method warps the image of the stressed state to fit the one of the relaxed state, note that both the underlying transformation model and the resulting displacement field are defined from relaxed to stressed state.

Regarding the similarity metric and the optimization strategy required for both the rigid and non-rigid registrations, we used the normalized correlation coefficient as the similarity metric and a stochastic gradient descent method with adaptive estimation of the step size as the optimizer [31].

Finally, we performed the image registration problem following a coarse-to-fine multiscale strategy, which allowed us to cope with different levels of matrix deformations while providing smooth displacement fields. Specifically, we used a three-level multiscale approach with 72 x 72 x 44 voxels, 36 x 36 x 22 voxels, and 18 x 18 x 11 voxels mesh size for the coarsest, intermediate and finest scales, respectively.

Removal of Errors caused by Engulfed Beads in Bead-based Displacement Fields

To ignore the beads engulfed by the cell and minimize errors in the calculation of the displacements, we supplied a binary mask of the segmented cell to the FFD-based image registration algorithm. To obtain the mask, the cell body was thresholded by Otsu's binarization algorithm.

While the cell mask ensures that engulfed beads are not corrupting the displacements adjacent to the cell surface, it does not prevent that non-zero displacements are recovered inside the cell body. This is

caused by the connected mesh used for FFD-based registration, which will propagate the mesh deformations located close to the cell surface to its surroundings, including the cell interior. Therefore, the final displacement field provided by the algorithm was reset to zero inside the cell mask.

Comparison of Cell-induced Displacement Fields

The displacement fields obtained from bead and fibril images were compared by calculating the difference in terms of displacement magnitude and direction at every spatial coordinate for every analyzed cell. Additionally, the mean and standard deviation of these differences were computed for a subset of displacements, namely those reaching at least 30% of the peak displacement magnitude for each particular cell.

Implementation

The computational workflow was implemented in MATLAB, except for FFD-based displacement field estimation, which was computed using Elastix [32], an open source multiplatform software for image registration. The integration of the elastix based FFD image registration on the main computational workflow was done as in [24]. The software program Paraview 4.3.1 (Kitware Inc., NY USA) was used for the 3D rendering of segmented cells and the visualization of 3D vector fields.

3. RESULTS

A schematic overview of the performed analyses is depicted in Figure 1, which summarizes the methodology followed for both sham experiments and cell-populated gels.

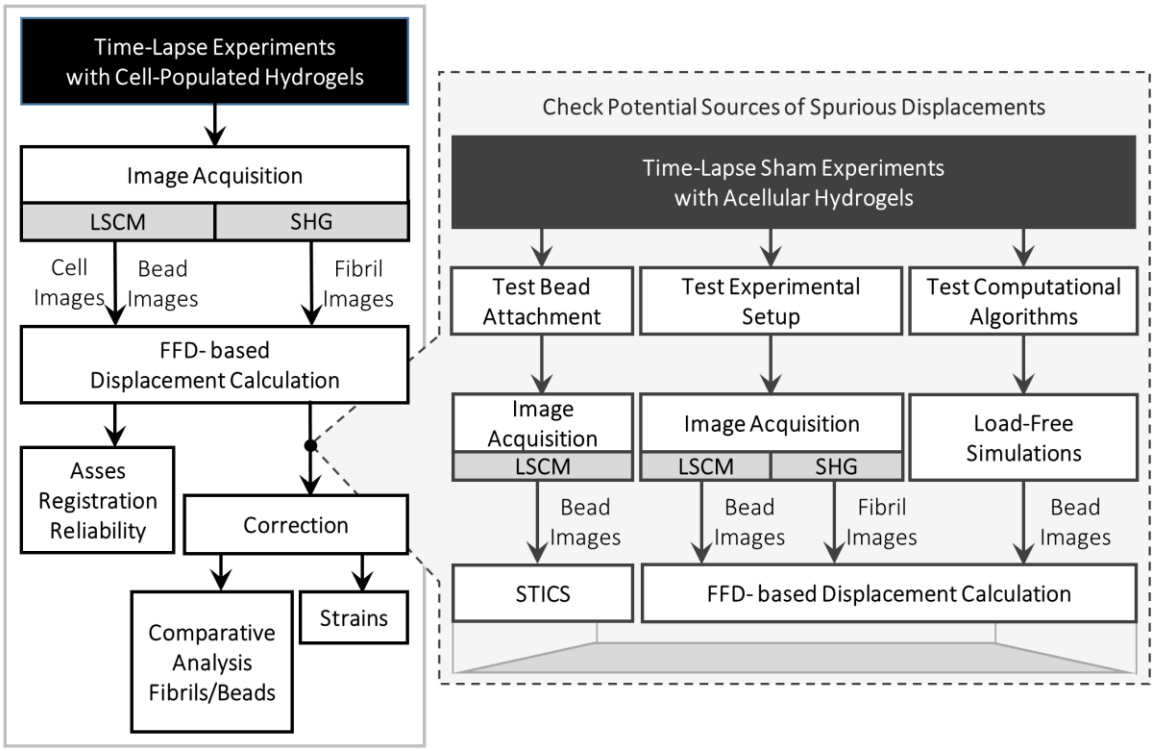

Figure 1. Schematic overview of the performed analyses and validations. LSCM: Laser Scanning Confocal Microscope; SHG: Second Harmonic Generation; FFD: Free Form Deformation; STICS: Spatio-Temporal Image Correlation Spectroscopy.

3.1. Sham Experiments show Spurious Displacement Patterns

For the correct interpretation of calculated displacements, it is important to verify to what extent the experimental setup and protocols as well as image registration procedures can give rise to spurious displacements that are not related to any cellular activity. In this regard, three different sham experiments were conducted.

First, the bead attachment to the fibrils was checked using image correlation spectroscopy to prevent errors induced by the motion of non-attached beads. Supplementary Figure S2 shows the spatial and temporal cross-correlation information for acquired time-series of beads embedded in the hydrogel. If beads would have moved during the time-lapse, the correlation peak would change over different time-lags (τ). Our results did not present the lateral shift (indicative of advected beads) or broadening of the correlation peak (indicative of diffusing beads) over different time-lags and thus confirm the attachment of beads.

Second, to rule out any dependency on experimental setup, protocol or personal handling, displacements were calculated from data acquired on two different setups from control hydrogels (without cells) prepared by various persons. Figure 2 (fibril-based images) and Supplementary Figure S3 (bead based images of the same specimen) show the resulting displacement maps for each vector component from data acquired on the main microscopy setup (as described in section 2.2). A spurious displacement pattern in the results provided by both fibrils and beads can be seen. Displacement magnitude varies smoothly with depth, but is rather constant within the imaging plane. When looking at the time lapses, we noticed that this pattern was present most of the time, however it was less evident at certain time points. Similar displacement patterns were observed for sham experiments conducted on the additional acquisition setup (Olympus BX61WI upright microscope; data not shown).

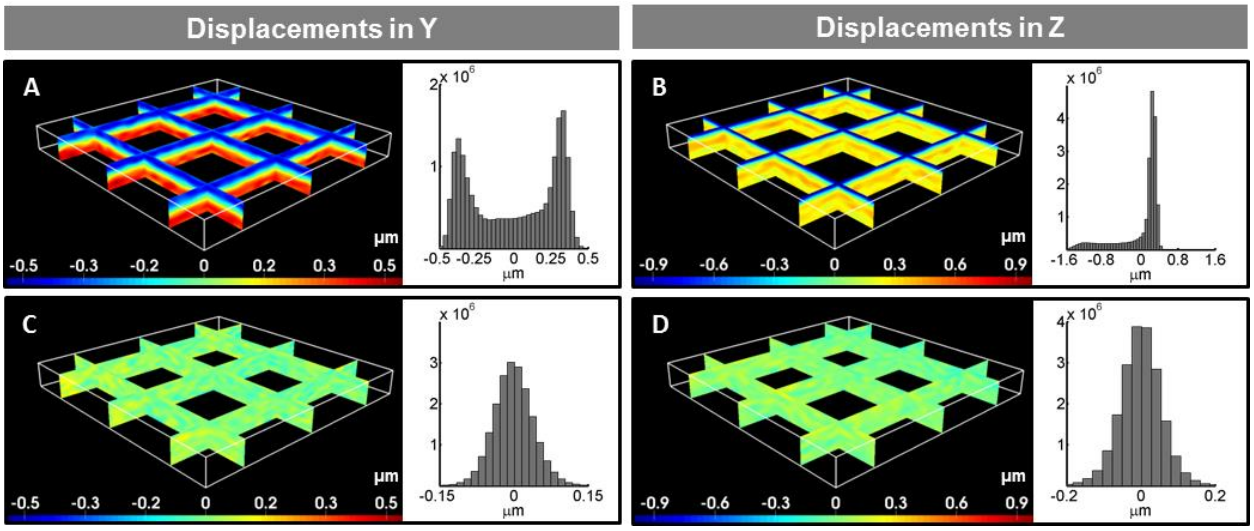

Figure 2. Spurious displacements obtained from fibril-based images in cell-free sham experiments, before (A, B) and after (C, D) correction. Axial cross-sections at multiple locations of the acquired volume and histograms (right insets) for the Y- (A) and Z- (B) components of the computed displacement field, and their corrected versions (C) and (D), respectively. Bounding box: 220 x 220 x 23 μm^3.

Third, we checked by using synthetic data if the observed spurious pattern of displacements was caused by an error in the algorithms used to compute the displacements. However, the displacements computed from the synthetic data were negligible (Supplementary Figure S4).

3.2. Spurious Displacement Patterns can be Corrected

We accounted for the spurious displacement pattern by calculating the average displacement vector for each XY-plane and subtracting it from the local displacement vector of each point in the corresponding plane. Histograms of the recovered displacements from the sham experiments, before and after the proposed correction, are shown on the right side of Figure 2 and Supplementary Figure S3. Whereas the spurious displacements presented a multimodal histogram, it became symmetric and unimodal after applying the correction, resembling a Gaussian-like random distribution of errors with zero mean. After

applying the described correction only negligible errors with standard deviation ~ 0.05 μm are found (Supplementary Figure S5), which is negligible compared to the displacements calculated in cell populated hydrogels and which were of the order of 1-10 µm after the correction (see also section 3.4). Additionally, the effectiveness of the correction method was evaluated on the displacements computed under cellular tractions. After correction, it can be observed (Figure 3) that the spurious displacement pattern is leveled out.

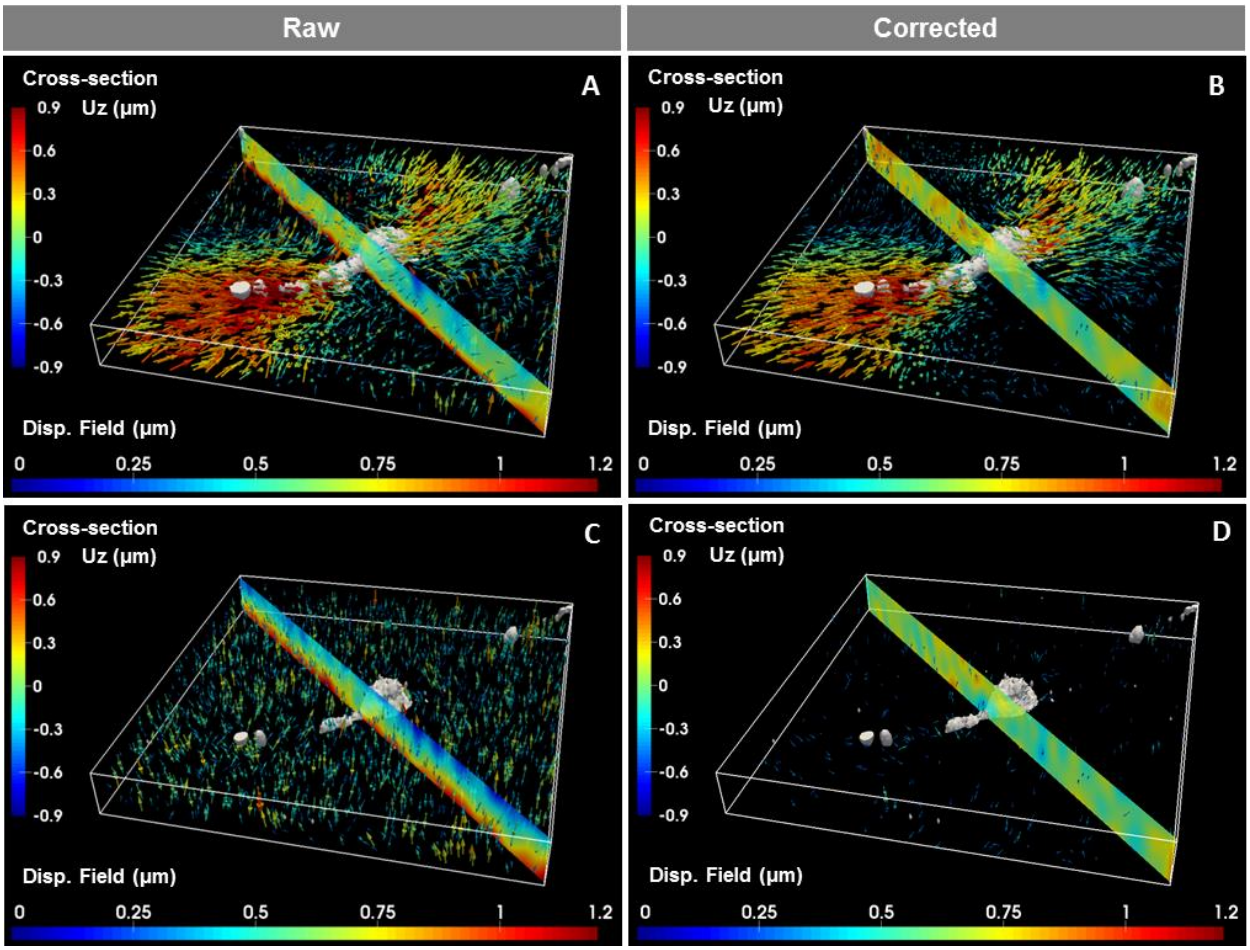

Figure 3. 3D displacements in cell-populated hydrogels before (A, C) and after (B, D) correction for spurious displacements computed from fibril-based images. Displacements are induced by a MRC-5 fibroblast (white) before (A,B) and 40 minutes after adding cytochalasin B (C,D). Displacement vector fields (arrows) and the Z-component (cross-section) of the displacements are shown simultaneously.

Note the different color scales for the Z-component in the cross-section ('Cross-section') and the displacement vector magnitude in the imaged region ('Disp. Field'). Bounding box: 170 x 170 x 21 μm^3.

3.3. Multiscale Free Form Deformation allows the Recovery of Large Deformations induced by MRC-5 Fibroblasts

To measure the deformations induced by MRC-5 fibroblasts embedded in collagen hydrogels, we imaged the collagen matrix around the cells with SHG microscopy before and after force relaxation with cytochalasin and evaluated the local displacement and strain fields via FFD-based image registration. As can be seen in Figure 4, these cells spread inside the hydrogel to an elongated and polarized configuration, while contracting the collagen hydrogel around their force poles located at the extremes of their principal axis resulting in a local alignment of the fibrils. This behavior was observed for cells embedded in both 2.4 mg/ml and 4.0 mg/ml hydrogels.

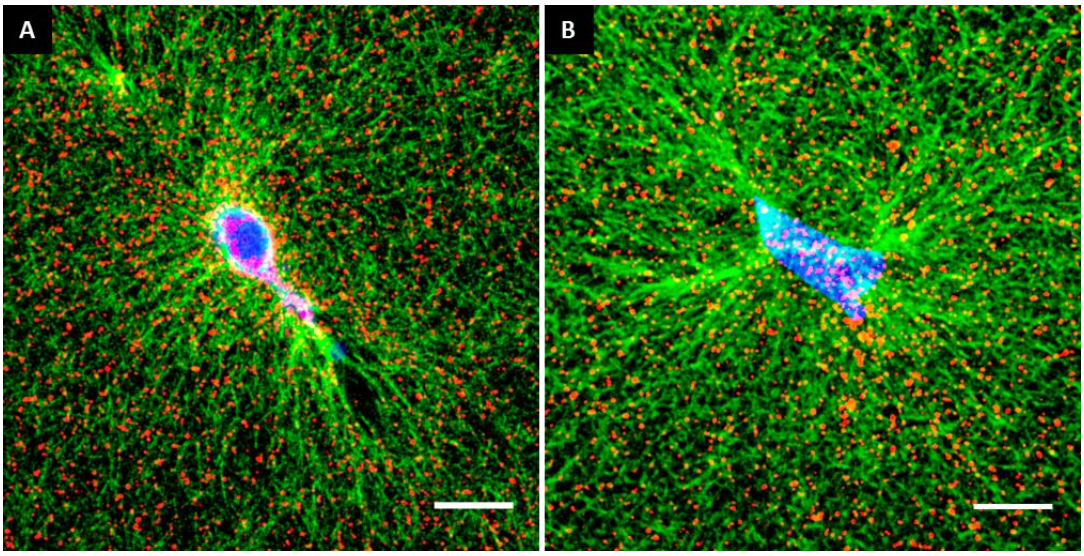

Figure 4. Cross-sections of 2.4 mg/ml (A) and 4.0 mg/ml (B) collagen hydrogels showing MRC-5 fibroblast (blue) induced alignment of fibrils (green) with a high density of fluorescent beads (red) attached. Beads engulfed or adsorbed by the cell are shown in magenta. Scale bar: 25 μm

The feasibility of FFD to register both fibril- and bead-based images was demonstrated for a number of representative cells (N=9 per collagen concentration). Figure 5 and Supplementary Figure S6 show fibril- (A) and bead-based (B) images in the unstressed (red) and stressed (green) hydrogels for collagen concentrations of 2.4 mg/ml and 4.0 mg/ml, respectively. After image registration they both (C and D) appear predominantly as yellow when the images in the unstressed and stressed state coincide. The latter registered images generated by the estimated deformations qualitatively show the success of the registration procedure and therefore the coherence and reliability of the computed displacements.

Once displacement fields are obtained (see section 3.4), any additional strain measure can be calculated. Here, we report results in terms of the Green-Lagrange strain tensor **E**, which is commonly used in nonlinear solid mechanics, and which is defined as:

$$\mathbf{E} = \tfrac{1}{2} (\mathbf{F}^T\mathbf{F} - \mathbf{I})$$

with **F** the deformation gradient tensor and **I** the identity tensor. Looking at example cells in Figures 6 and S7, strain components up to 40% are calculated near the cell's force poles, demonstrating the existence of large strains for both 2.4 mg/ml and 4.0 mg/ml collagen concentrations. Taken together Figures 5 and 6 and Supplementary Figures S6 and S7, FFD proves to be successful in registering fibril-based and bead-based images, even for large deformation conditions and dense fibrillar networks.

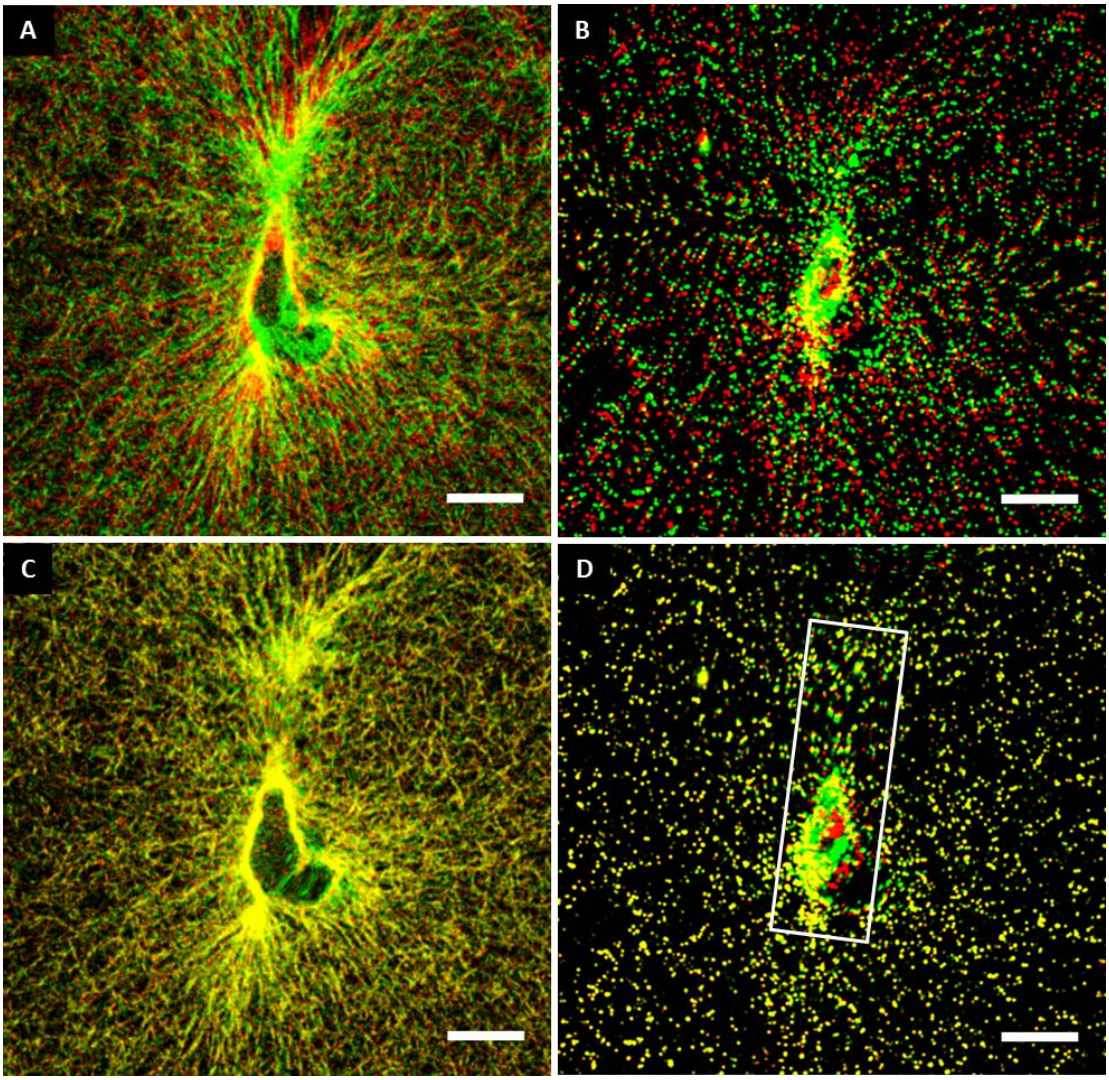

Figure 5. FFD-based image registration of the unstressed (84 minutes after addition of cytochalasin B) and stressed (before addition of cytochalasin B) gel with 2.4 mg/ml collagen concentration. Pseudo-colored cross-sections of the collagen hydrogel showing the fibril- (A) and bead-based (B) images before the registration, and their registered results (C) and (D), respectively, that lead to the recovered displacement field. The fibrils/beads in the unstressed and stressed hydrogel are pseudo-colored in red and green, respectively. Fibrils/beads appear as yellow where both the unstressed and stressed conditions match. The beads engulfed by the cell are ignored during the registration process (D, delineated area) to avoid artifacts in the recovered displacements. Scale bars: 25 μm.

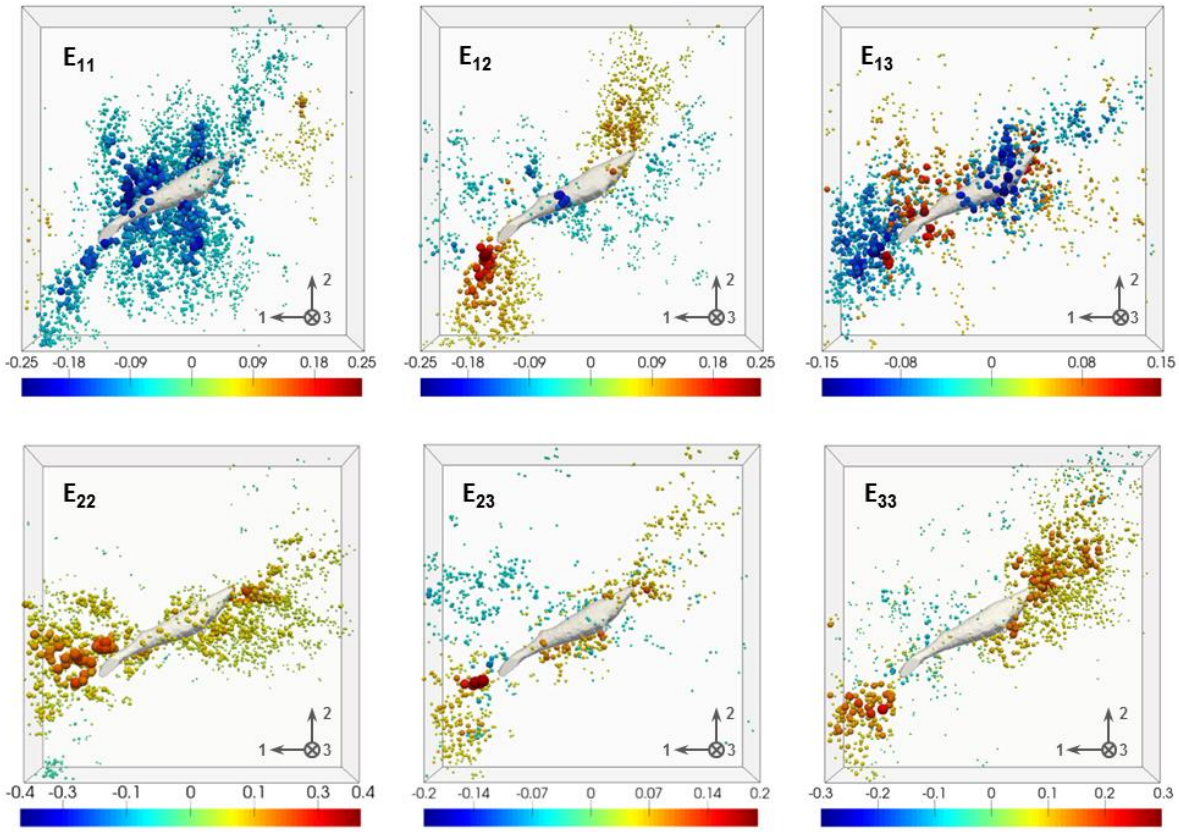

Figure 6. Symmetric Green-Lagrange strain tensor for a sample cell in 2.4 mg/ml collagen depicted in Figure S8A. The maps have been uniformly sampled at random locations to allow the 3D visualization of each component of the tensor.

3.4. Both Fibrils and Beads provide Comparable Displacement Fields

Using external markers, such as fluorescent beads, to track displacements implies several drawbacks, as mentioned in the introduction. In this regard, we comparatively examined whether identical displacement fields can be derived from bead- and fibril-based images acquired by Second Harmonic Generation.

The results are shown in Figure 7, Supplementary Figures S8 and S9 and Supplementary Video 1. A qualitative comparison of the results does not reveal substantial differences between both fields in

terms of distribution, orientation or magnitude of the displacements for cells embedded in both 2.4 mg/ml and 4.0 mg/ml collagen gels. Maximum displacements were typically ~6 µm, ranged between 1.2 and 14 µm, and were located near the cell's poles. Of the two poles, the one that displayed the most 'pointed' (slender) shape was associated to the overall maximum displacement. Displacement vectors were pointing towards the cells' center, suggesting contractile forces. Displacement fields were found to be anisotropic, with largest displacements along the direction of cell elongation, i.e. aligned with the cell's polarity.

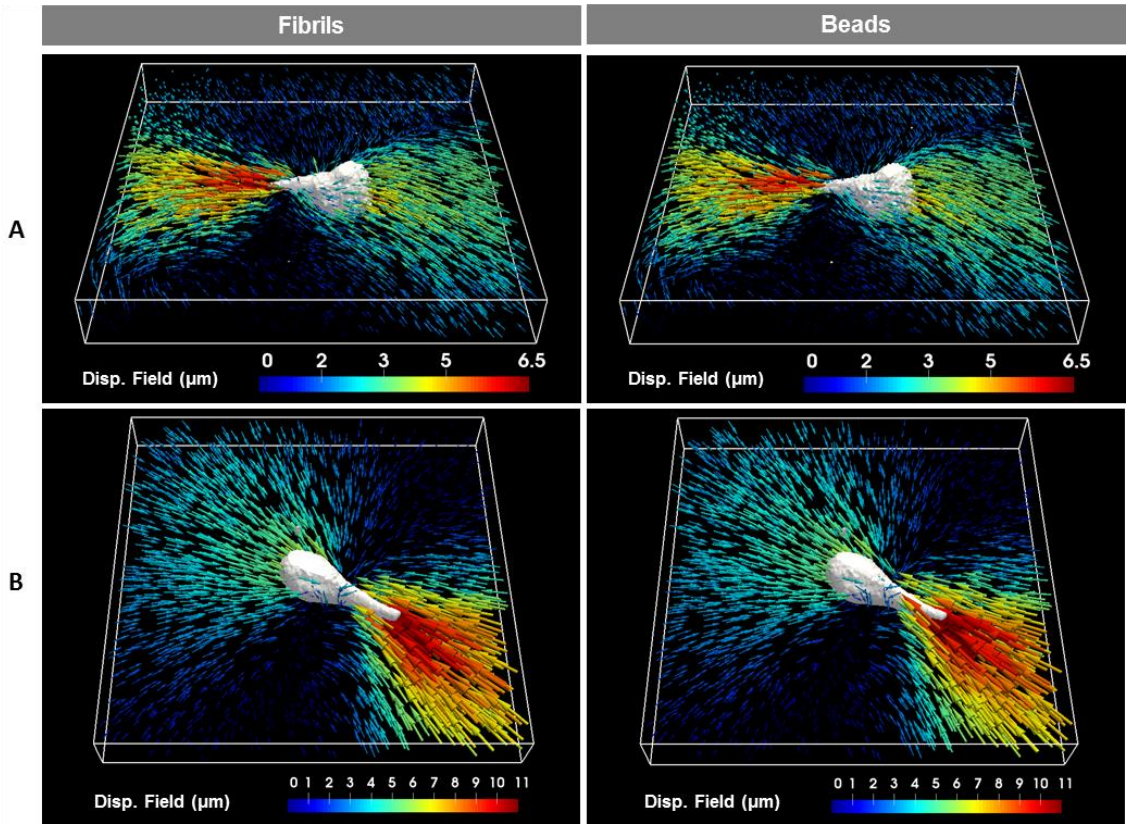

Figure 7. Representative 3D displacements induced by 2 different MRC-5 fibroblasts embedded in 2.4 mg/ml (A) and 4.0 mg/ml(B) collagen, respectively. Displacement fields were obtained from the registration of fibril-based images (left column) and bead-based images (right column). Bounding box: 170 μm x 170 μm x 24 μm (A) and 170 x 170 x 23 μm^3 (B).

To quantitatively compare the retrieved displacement fields from both bead- and fibril-based images, we computed the relative difference (in %) between their displacement magnitudes and the absolute difference (degrees) between their direction at every spatial coordinate (Figures 8 and 9 A,B and Supplementary Figures 10 and 11). These results show relatively low differences in general, with mean and standard deviation values for the magnitude in the range of -6 to 3 and 4 to 15 %, respectively; and with mean and standard deviation values for the direction in the range of 3 to 11 and 2 to 8 degrees, respectively. As expected, relative differences tend to increase for small displacement magnitudes, because of the small denominator. As in general, one is more interested in regions of large displacements (which are found near the cell-hydrogel interface), further quantitative analysis was restricted to points that exhibited a displacement magnitude larger than the 30% of the peak value for that cell (as estimated from the bead data, which was used as the reference). Figures 8 C,D and 9 C,D summarize the numerical results for each cell embedded in 2.4 mg/ml and 4.0 mg/ml collagen gels, respectively, displaying relatively low quantitative differences between the displacements computed from fibril- and bead-based images, both in terms of magnitude and orientation.

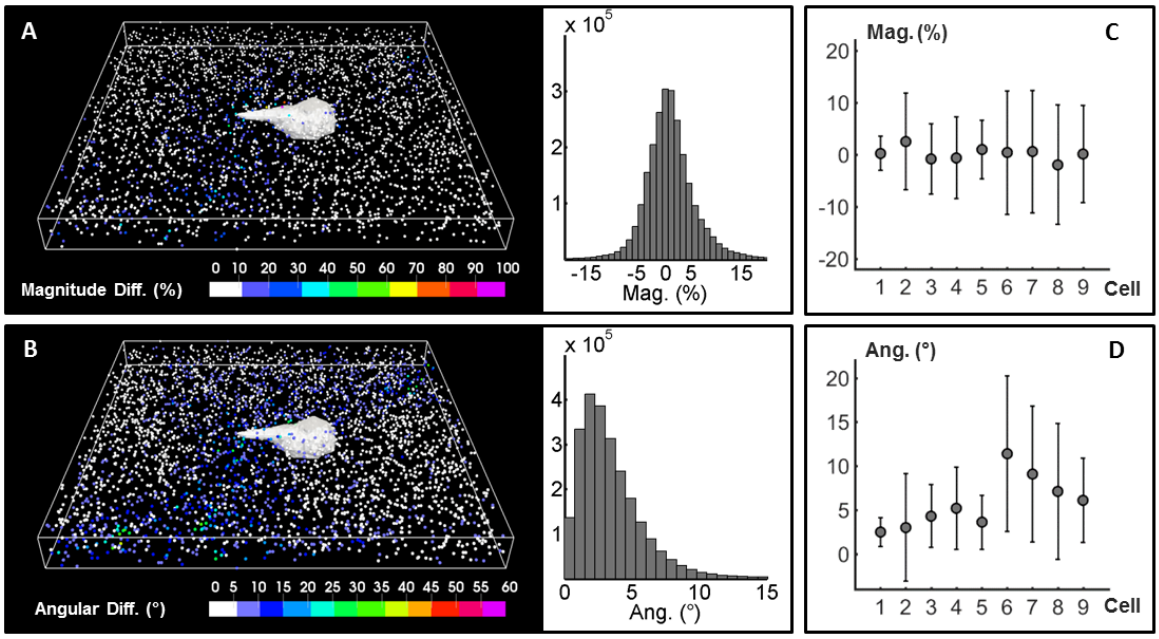

Figure 8. Quantitative comparison between the displacements computed from fibril- and bead-based images for cells in 2.4 mg/ml collagen gels. Map of the relative difference (%) between displacement magnitudes (A) and the angle (degrees) between displacement vector directions (B) for the displacement fields in Figure 7A. The map is uniformly sampled at random locations to allow the 3D visualization of the differences for the whole volume. Histograms of the differences (right insets) are computed from those regions exhibiting a displacement magnitude larger than 30% of its peak value. Mean differences (± standard deviation) between the fibril- and bead-based displacements for nine different cells (C,D).

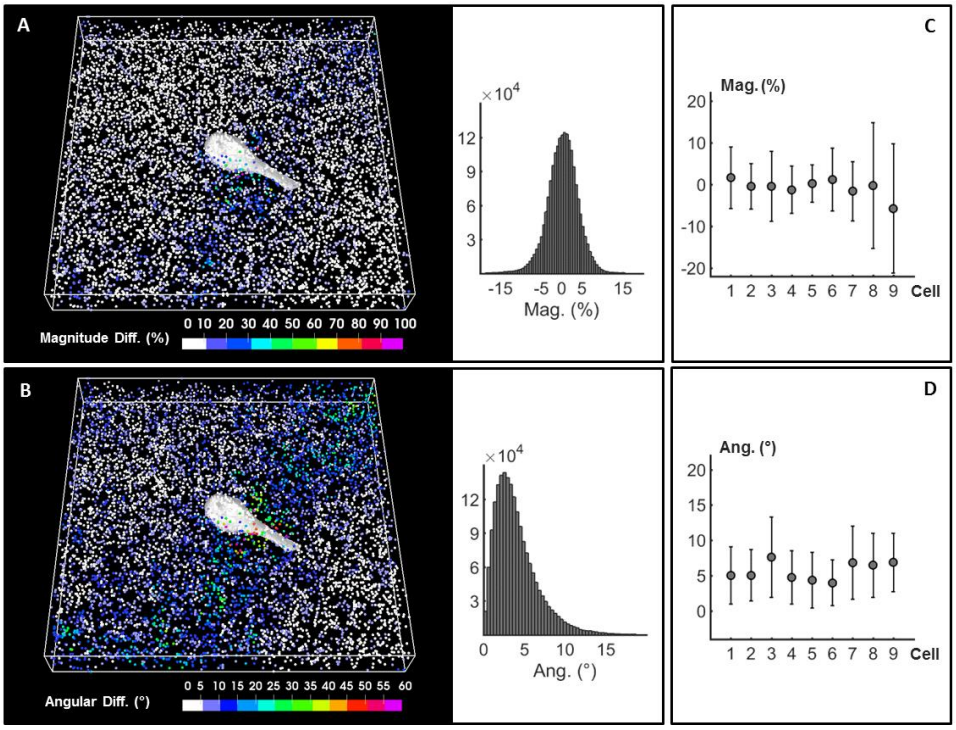

Figure 9. Quantitative comparison between the displacements computed from fibril- and bead-based images for cells in 4.0 mg/ml collagen gels. Map of the relative difference (%) between displacement magnitudes (A) and the angle (degrees) between displacement vector directions (B) for the displacement fields in Figure 7B. The map is uniformly sampled at random locations to allow the 3D visualization of the differences for the whole volume. Histograms of the differences (right insets) are computed from those regions exhibiting a displacement magnitude larger than 30% of its peak value.

Mean differences (± standard deviation) between the fibril- and bead-based displacements for nine different cells (C,D).

4. DISCUSSION

In this paper, we have compared two approaches to quantify large deformations induced by MRC-5 human lung fibroblasts in fibrillar type I collagen hydrogels of different concentrations. Sham experiments revealed a spurious pattern of displacements not originating from cellular activity. As the same pattern was observed in the displacements computed from both beads and fibrils, its origin cannot be attributed to any of them. Also, the used image registration algorithms, the specifics of our experimental protocols and equipment as source of the spurious displacements were excluded by using synthetic data and repeating the experiments under different conditions. Note that the pattern was observed for each displacement component independently. Recently, a depth-dependent lateral shift in the apparent position of a fluorescent point source, termed wobble effect, has been reported [33]. This wobble is caused by both the coverslip tilt and the aberrations introduced by the microscope system, producing a distortion effect that resembles the pattern we noticed in the X- and Y-components of the displacement fields computed from our sham experiments. Analogously to our results, the wobble effect has been reported for microscopes and objectives from different manufacturers with varying magnitude and direction, resulting in a microscope-dependent distortion. However, contrary to our results, the wobble effect is supposed to remain stable in time under similar imaging conditions and thus, other effects may have contributed to our spurious displacement pattern as well. The pattern of the Z-component of the displacements may have been caused by slight imprecisions in the vertical positioning of the image acquisition system. This source of misalignment has already been suggested by Steinwachs et al [16]. Different from our correction method, they pre-corrected acquired z-stacks before

the calculation of the cell-induced displacements, which produced slightly low-pass filtered images that would attenuate the artefactual displacement distribution we detected in our sham experiments.

As the spurious displacements observed in the control experiments are likely to be present in the real experiments with cell-populated hydrogels as well, it is necessary to correct for them. The correction can easily be done by calculating the average displacement vector for each XY-plane and subtracting it from the local displacement vector of each point in the corresponding plane. After correction, the spurious displacement pattern is leveled out, in both control experiments and experiments with cells.

FFD-based non-rigid image registration was used to calculate the displacement fields generated by the MRC-5 fibroblasts. As we previously showed [24], this technique provides a powerful alternative to capture a wide range of locally non-uniform displacements overcoming most of the limitations inherent to other methods. Indeed, it does not rely on tracking fluorescent beads and it can be intuitively viewed as an enhanced version of the block-matching PIV method. Furthermore, whereas previous efforts to estimate the deformations of fibrillar networks directly from fibril-based images were mainly limited to relatively small displacements (order of 1-2 μm, [16] and [22]) and strains (less than 10%, [22]), we have shown here that multiscale FFD can be used to consistently recover large displacements (of the order of 10 μm), large strains (shown here up to 40%) and any complexity associated to this. Therefore, FFD provides a versatile solution to reliably quantify displacements in TFM experiments that deal with large deformation regimes.

The displacement fields that were induced by human lung fibroblasts looked qualitatively similar to those reported for elongated, polarized breast carcinoma cells in fibrillar collagen gels [16,22] in the sense that they were all aligned with the cell's polarity and the result of mostly contractile forces. As

mentioned in the previous paragraph magnitudes of displacements and strains were much higher in our experiments. Given the fact that collagen concentrations used in this work were of the same order of magnitude (2-4 mg/ml) for all these studies, it seems likely that differences can be at least partially attributed to the difference in cell type.

Finally, our comparative study of cell-induced deformations exposed negligible differences between the displacements computed from beads and fibrils. These differences were assessed both qualitatively from the visual inspection of recovered displacements (Figures 7, S8 and S9) and quantitatively (Figures 8, 9, S10 and S11), showing average differences in magnitude and angle that were typically of less than 10 % and less than 10 degrees, respectively. It is important to remark that the equivalence between the displacements computed from beads and fibrils would remain valid only under the following conditions. First, the algorithm used for the recovery of the matrix displacements should be capable of cancelling out the potential effects derived from the motion of beads engulfed by the cells. Second, the bead density should be high enough to comply with the Nyquist sampling theorem and thus, a large number of beads need to be bound to collagen fibrils. Indeed, compared to previously reported bead densities [34], our setup presented a 5-fold reduction in bead-bead distance, with average values of ~4.8 μm. Note that for cells inducing highly varying (non-uniform) displacement patterns in space, lower bead densities will lead to a loss of the high frequency content, affecting the estimated displacement magnitudes and spreading them over larger volumes, *i.e.* reducing their spatial resolution. Apart from these conditions, selecting between fibrils and beads to compute the displacement field in TFM experiments will also depend on specific experimental requirements. For instance, while fibrillar networks can be fluorescently labeled, they can also be imaged by label-free techniques such as confocal reflection microscopy [16,22], and SHG as done here, providing an extra available channel that can be used to simultaneously acquire other fluorescently labelled cellular structures related to cell force generation, such as the cell's actin cytoskeleton. Moreover, fibril images provide structural

information and how the cells may remodel the fibrillar structure of a biomaterial, which can be an important determinant of cell fate [25]. Finally, the use of beads may have an impact on the mechanical properties of the biomaterial or on cell behavior, *e.g.* due to bead engulfment.

5. CONCLUSION

In conclusion, this novel approach combines non-rigid image registration with label-free SHG imaging and enables the recovery of complex and large deformations induced by cells in fibrillar environments. It is a straightforward technique, without the need of conventionally used fluorescent beads, with all their drawbacks. Comparison to bead-based imaging revealed a good qualitative and quantitative correspondence between fibril-based and bead-based displacement fields. The ability to recover complex and large deformations broadens the applicability in the fast growing field of traction force microscopy. Additionally, it may also advance biomaterial and tissue engineering studies where large cell-induced matrix displacements are part of cell-biomaterial interactions and cell-mediated biomaterial remodelling in soft fibrillar materials.

ASSOCIATED CONTENT

Supporting Information

Supplemental notes, figures and video.

AUTHOR INFORMATION

Corresponding Author

* (H.V.O) E-mail: hans.vanoosterwyck@kuleuven.be. Phone: +3216-327-067.

* (M.A.) E-mail: marcel.ameloot@uhasselt.be. Phone: +3211-269-233.

Author Contributions

‡These authors contributed equally. H.B., A.J.P., M.A. and H.V.O. jointly designed the experiments. H.B. performed all experiments. A.J.P. analyzed all experiments. K.S. assisted with the hydrogel fabrication. M.V. performed sham experiments at the additional microscope setup. C.S. and M.R. gave their technical support during data collection. The manuscript was written through contributions of all authors. All authors have given approval to the final version of the manuscript.

Notes

The authors declare no competing financial interests.

Acknowledgements

H.B. acknowledges funding from Research Foundation Flanders (Fonds Wetenschappelijk Onderzoek, FWO) for a doctoral fellowship: 11ZB115N. C.S. acknowledges funding from Research Foundation Flanders (Fonds Wetenschappelijk Onderzoek, FWO) for a postdoctoral fellowship. The authors also thank FWO for the research grants G0821.13 and G.0B96.15.

H.V.O. acknowledges that the research leading to these results has received funding from the European Research Council under the European Union's Seventh Framework Programme (FP7/2007-2013)/ ERC Grant Agreement n° 308223). M.A. thanks the Province of Limburg (Belgium) for the financial support within the tUL IMPULS FASE II program, allowing for the upgrading of the laser source used in this work. Prof. M. vandeVen is acknowledged for his theoretical support. H.B. gratefully acknowledges the assistance of Mrs. P. Bex.

REFERENCES

[1] E. Cukierman, R. Pankov, D.R. Stevens, K.M. Yamada, Taking cell-matrix adhesions to the third dimension., Science. 294 (2001) 1708–12. doi:10.1126/science.1064829.

[2] F. Pampaloni, E.G. Reynaud, E.H.K. Stelzer, The third dimension bridges the gap between cell culture and live tissue., Nat. Rev. Mol. Cell Biol. 8 (2007) 839–845. doi:10.1038/nrm2236.

[3] D. Loessner, K.S. Stok, M.P. Lutolf, D.W. Hutmacher, J.A. Clements, S.C. Rizzi, Bioengineered 3D platform to explore cell-ECM interactions and drug resistance of epithelial ovarian cancer cells, Biomaterials. 31 (2010) 8494–8506. doi:10.1016/j.biomaterials.2010.07.064.

[4] T. Mammoto, D.E. Ingber, Mechanical control of tissue and organ development., Development. 137 (2010) 1407–1420. doi:10.1242/dev.024166.

[5] P.M. Gilbert, K.L. Havenstrite, K.E.G. Magnusson, A. Sacco, N. a Leonardi, P. Kraft, N.K. Nguyen, S. Thrun, M.P. Lutolf, H.M. Blau, Substrate elasticity regulates skeletal muscle stem cell self-renewal in culture. (Supplementary), Science. 329 (2010) 1078–81. doi:10.1126/science.1191035.

[6] S.P. Carey, C.M. Kraning-Rush, R.M. Williams, C.A. Reinhart-King, Biophysical control of invasive tumor cell behavior by extracellular matrix microarchitecture, Biomaterials. 33 (2012) 4157–4165. doi:10.1016/j.biomaterials.2012.02.029.

[7] N. Huebsch, P.R. Arany, A.S. Mao, D. Shvartsman, O. a Ali, S. a Bencherif, J. Rivera-Feliciano, D.J. Mooney, Harnessing traction-mediated manipulation of the cell/matrix interface to control stem-cell fate., Nat. Mater. 9 (2010) 518–26. doi:10.1038/nmat2732.

[8] M.P. Lutolf, P.M. Gilbert, H.M. Blau, Designing materials to direct stem-cell fate., Nature. 462 (2009) 433–41. doi:10.1038/nature08602.

[9] K. Ghosh, Z. Pan, E. Guan, S. Ge, Y. Liu, T. Nakamura, X.-D. Ren, M. Rafailovich, R.A.F. Clark, Cell adaptation to a physiologically relevant ECM mimic with different viscoelastic properties., Biomaterials. 28 (2007) 671–9. doi:10.1016/j.biomaterials.2006.09.038.

[10] K. Bott, Z. Upton, K. Schrobback, M. Ehrbar, J.A. Hubbell, M.P. Lutolf, S.C. Rizzi, The effect of matrix characteristics on fibroblast proliferation in 3D gels, Biomaterials. 31 (2010) 8454–8464. doi:10.1016/j.biomaterials.2010.07.046.

[11] J.H. Wang, B. Li, The principles and biological applications of cell traction force microscopy, World. 29 (2010) 449–458. http://www.formatex.info/microscopy4/449-458.pdf (accessed December 4, 2012).

[12] T. Oliver, M. Dembo, K. Jacobson, Traction forces in locomoting cells., Cell Motil. Cytoskeleton. 31 (1995) 225–40. doi:10.1002/cm.970310306.

[13] M. Dembo, T. Oliver, a Ishihara, K. Jacobson, Imaging the traction stresses exerted by locomoting cells with the elastic substratum method., Biophys. J. 70 (1996) 2008–22. doi:10.1016/S0006-3495(96)79767-9.

[14] J. Lee, M. Leonard, T. Oliver, A. Ishihara, K. Jacobson, Traction Forces Generated by Locomoting Keratocytes, J. Cell Biol. 127 (1994) 1957–1964.

[15] W.R. Legant, J.S. Miller, B.L. Blakely, D.M. Cohen, G.M. Genin, C.S. Chen, Measurement of mechanical tractions exerted by cells in three-dimensional matrices., Nat. Methods. 7 (2010) 969–71. doi:10.1038/nmeth.1531.

[16] J. Steinwachs, C. Metzner, K. Skodzek, N. Lang, I. Thievessen, C. Mark, S. Münster, K.E. Aifantis, B. Fabry, Three-dimensional force microscopy of cells in biopolymer networks., Nat. Methods. 13 (2016) 171–176. doi:10.1038/nmeth.3685.

[17] D.A. Stout, E. Bar-Kochba, J.B. Estrada, J. Toyjanova, H. Kesari, J.S. Reichner, C. Franck, Mean deformation metrics for quantifying 3D cell–matrix interactions without requiring information about matrix material properties, Proc. Natl. Acad. Sci. 113 (2016) 2898–2903. doi:10.1073/pnas.1510935113.

[18] S.J. Han, Y. Oak, A. Groisman, G. Danuser, Traction microscopy to identify force modulation in subresolution adhesions., Nat. Methods. 12 (2015) 653–656. doi:10.1038/nmeth.3430.

[19] I.M. Tolić-Nørrelykke, J.P. Butler, J. Chen, N. Wang, Spatial and temporal traction response in human airway smooth muscle cells., Am. J. Physiol. Cell Physiol. 283 (2002) C1254-66. doi:10.1152/ajpcell.00169.2002.

[20] B. Sabass, M.L. Gardel, C.M. Waterman, U.S. Schwarz, High resolution traction force microscopy based on experimental and computational advances., Biophys. J. 94 (2008) 207–20. doi:10.1529/biophysj.107.113670.

[21] H. Colin-York, D. Shrestha, J.H. Felce, D. Waithe, E. Moeendarbary, S.J. Davis, C. Eggeling, M. Fritzsche, Super-Resolved Traction Force Microscopy (STFM), Nano Lett. 16 (2016) 2633–2638. doi:10.1021/acs.nanolett.6b00273.

[22] J. Kim, C.A.R. Jones, N.S. Groves, B. Sun, Three-dimensional reflectance traction microscopy, PLoS One. 11 (2016) 1–17. doi:10.1371/journal.pone.0156797.

[23] E. Bar-Kochba, J. Toyjanova, E. Andrews, K.S. Kim, C. Franck, A Fast Iterative Digital Volume Correlation Algorithm for Large Deformations, Exp. Mech. C (2014) 261–274. doi:10.1007/s11340-014-9874-2.

[24] A. Jorge-Peñas, A. Izquierdo-Alvarez, R. Aguilar-Cuenca, M. Vicente-Manzanares, J.M. Garcia-Aznar, H. Van Oosterwyck, E.M. De-Juan-Pardo, C. Ortiz-De-Solorzano, A. Muñoz-Barrutia, Free

form deformation-based image registration improves accuracy of traction force microscopy, PLoS One. 10 (2015) 1–22. doi:10.1371/journal.pone.0144184.

[25] K. Sanen, R. Paesen, S. Luyck, J. Phillips, I. Lambrichts, W. Martens, M. Ameloot, Label-free mapping of microstructural organisation in self-aligning cellular collagen hydrogels using image correlation spectroscopy, Acta Biomater. 30 (2016) 258–264. doi:10.1016/j.actbio.2015.10.047.

[26] F.S. Pavone, P.J. Campagnola, Second harmonic generation imaging, 2013.

[27] P.W. Wiseman, Image correlation spectroscopy: Mapping correlations in space, time, and reciprocal space, Methods Enzymol. 518 (2013) 245–267. doi:10.1016/B978-0-12-388422-0.00010-8.

[28] B. Hebert, S. Costantino, P.W. Wiseman, Spatiotemporal image correlation spectroscopy (STICS) theory, verification, and application to protein velocity mapping in living CHO cells., Biophys. J. 88 (2005) 3601–3614. doi:10.1529/biophysj.104.054874.

[29] A. Jorge-Peñas, A. Muñoz-Barrutia, E.M. De-Juan-Pardo, C. Ortiz-de-Solorzano, Validation tool for traction force microscopy., Comput. Methods Biomech. Biomed. Engin. (2014) 37–41. doi:10.1080/10255842.2014.903934.

[30] D. Garcia, Robust smoothing of gridded data in one and higher dimensions with missing values, Comput. Stat. Data Anal. 54 (2010) 1167–1178. doi:10.1016/j.csda.2009.09.020.

[31] S. Klein, J.P.W. Pluim, M. Staring, M. a. Viergever, Adaptive stochastic gradient descent optimisation for image registration, Int. J. Comput. Vis. 81 (2009) 227–239. doi:10.1007/s11263-008-0168-y.

[32] S. Klein, M. Staring, K. Murphy, M. a Viergever, J.P.W. Pluim, Elastix: a Toolbox for Intensity-

Based Medical Image Registration., IEEE Trans. Med. Imaging. 29 (2010) 196–205. doi:10.1109/TMI.2009.2035616.

[33] L. Carlini, S.J. Holden, K.M. Douglass, S. Manley, Correction of a depth-dependent lateral distortion in 3D super-resolution imaging, PLoS One. 10 (2015) 1–15. doi:10.1371/journal.pone.0142949.

[34] T.M. Koch, S. Münster, N. Bonakdar, J.P. Butler, B. Fabry, 3D Traction forces in cancer cell invasion., PLoS One. 7 (2012) e33476. doi:10.1371/journal.pone.0033476.

Supplementary Notes

Note 1: Brief explanation Image Correlation Spectroscopy

All image correlation spectroscopy variants are based on the analysis of fluorescence fluctuations measured within an observation area. The fluctuations of fluorescence intensity, δ_i, recorded in the image series are defined as:

$$\delta_i(x,y,t) = i(x,y,t) - \langle i(x,y,t)\rangle_{XY}$$

where $\langle\ldots\rangle_{XY}$ denotes spatial averaging of the stack of images; *x* and *y* represent spatial coordinates of the considered pixel, *t* is the time of the considered image in the time series, and $i(x,y,t)$ indicates the intensity at (x,y) and time *t*.

The fluctuations can be defined as temporal intensity fluctuations between images taken at different times in a time lapse (*i.e.* temporal image correlation spectroscopy*;* TICS) and spatial intensity fluctuations across a given image (*i.e.* spatio-temporal image correlation spectroscopy; STICS). The spatial fluctuations include changes in the number of static or slowly moving fluorophores in space, while temporal fluctuations reflect dynamic variations in the amount of fluorophores at a given spot over time since the fluorescent molecules undergo transport.

TICS can be employed for measuring the magnitude of the diffusion coefficient and/or flow speed of slowly moving particles from an image time lapse [1–3]. To obtain a single temporal autocorrelation function $G(0,0,\tau)$, all autocorrelation functions yielding from each pixel location are averaged:

$$G(0,0,\tau) = \left\langle \frac{\langle \delta_i(x,y,t)\ \delta_i(x,y,t+\tau)\rangle_{XY}}{\langle i(x,y,t)\rangle_{XY}\ \langle i(x,y,t+\tau)\rangle_{XY}} \right\rangle_T$$

where <…> indicates the averaging of all images in space ($_{XY}$) or time ($_T$); and τ denotes the time-lag.

In STICS, the spatial information derived from the two-dimensional spatial correlations is combined with the time-dependent transport measured using the temporal correlation. The average correlation function for all time-lag τ separated pairs of images is represented by $G(\xi,\eta,\tau)$ [3,4]:

$$G(\xi,\eta,\tau) = \left\langle \frac{\langle \delta_{i(x,y,t)}\ \delta_i(x+\xi,y+\eta,t+\tau)\rangle_{XY}}{\langle i(x,y,t)\rangle_{XY}\ \langle i(x+\xi,y+\eta,t+\tau\rangle_{XY}} \right\rangle_T$$

where ξ and η denote the spatial lag variables in *x* and *y,* respectively.

Supplementary Figures

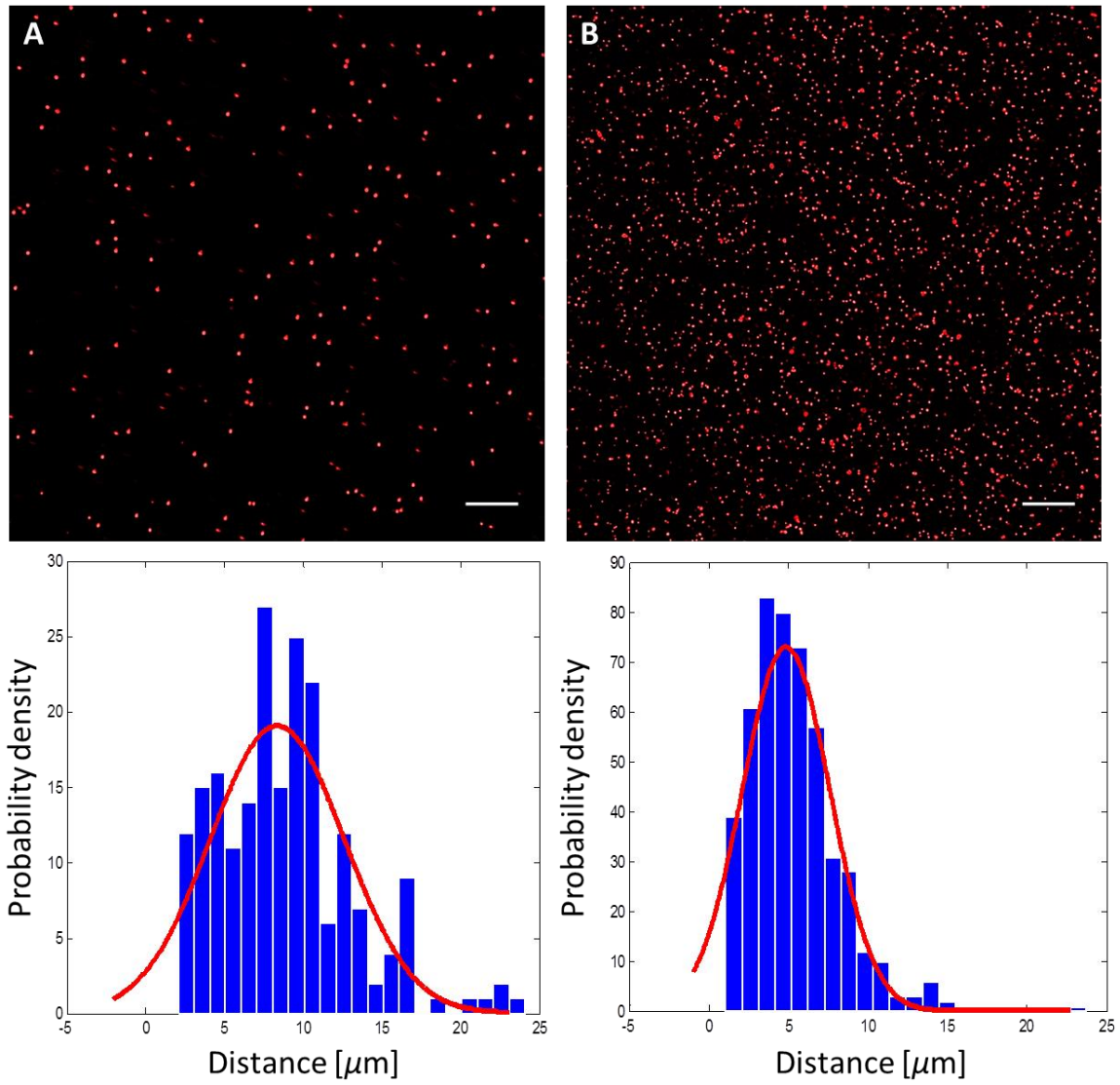

Figure S1. Confocal section and nearest neighbour bead-bead distance distribution histogram of **(A)** 1 µm and **(B)** 200 nm fluorescent beads inside the collagen type I hydrogel. Scale bars: 20 μm.

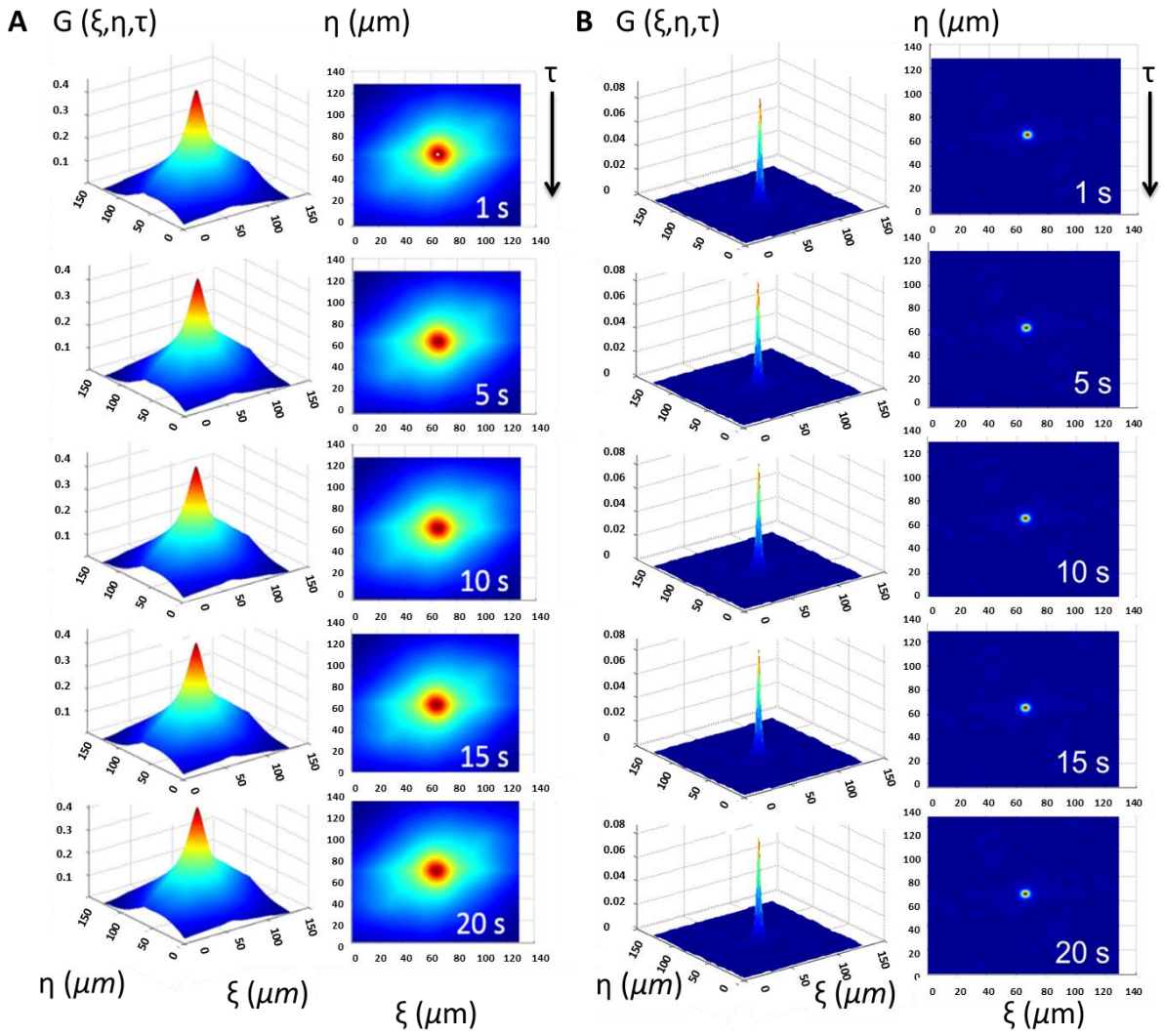

Figure S2. Evaluation of the attachment of 1 μm **(A)** and 0.2 μm **(B)** fluorescent beads to the collagen type I fibrils by spatiotemporal image correlation spectroscopy. No broadening or lateral shift of the correlation peak is observed, indicating that there is no diffusion or flow of the beads.

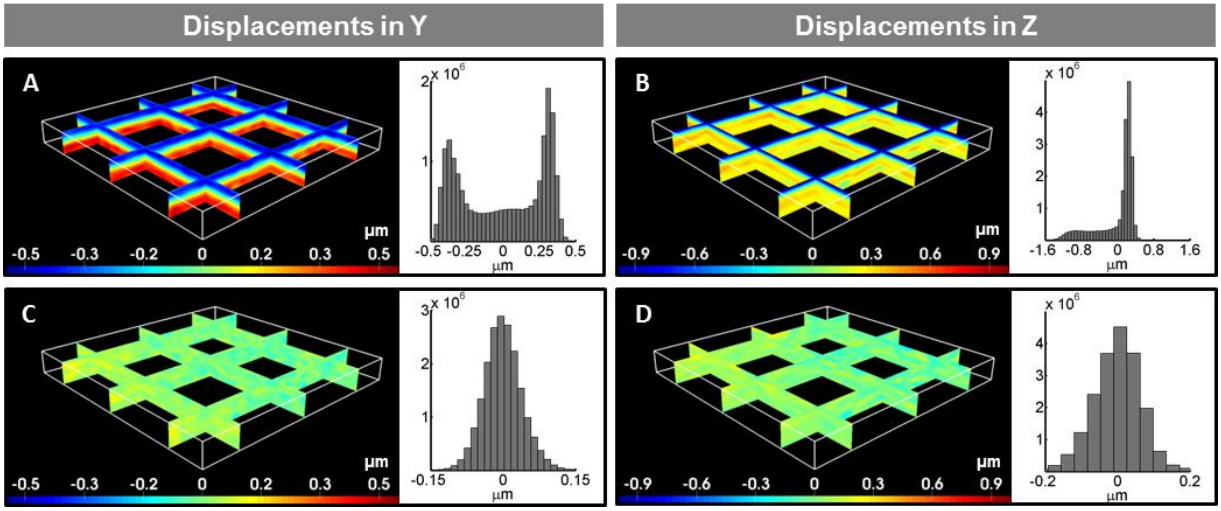

Figure S3. Spurious displacements obtained from bead-based images in cell-free sham experiments, before (A, B) and after (C, D) correction. Axial cross-sections at multiple locations of the acquired volume and histograms (right insets) for the Y- (A) and Z- (B) components of the computed displacement field, and their corrected versions (C) and (D), respectively. Bounding box: 220 x 220 x 23 μm^3.

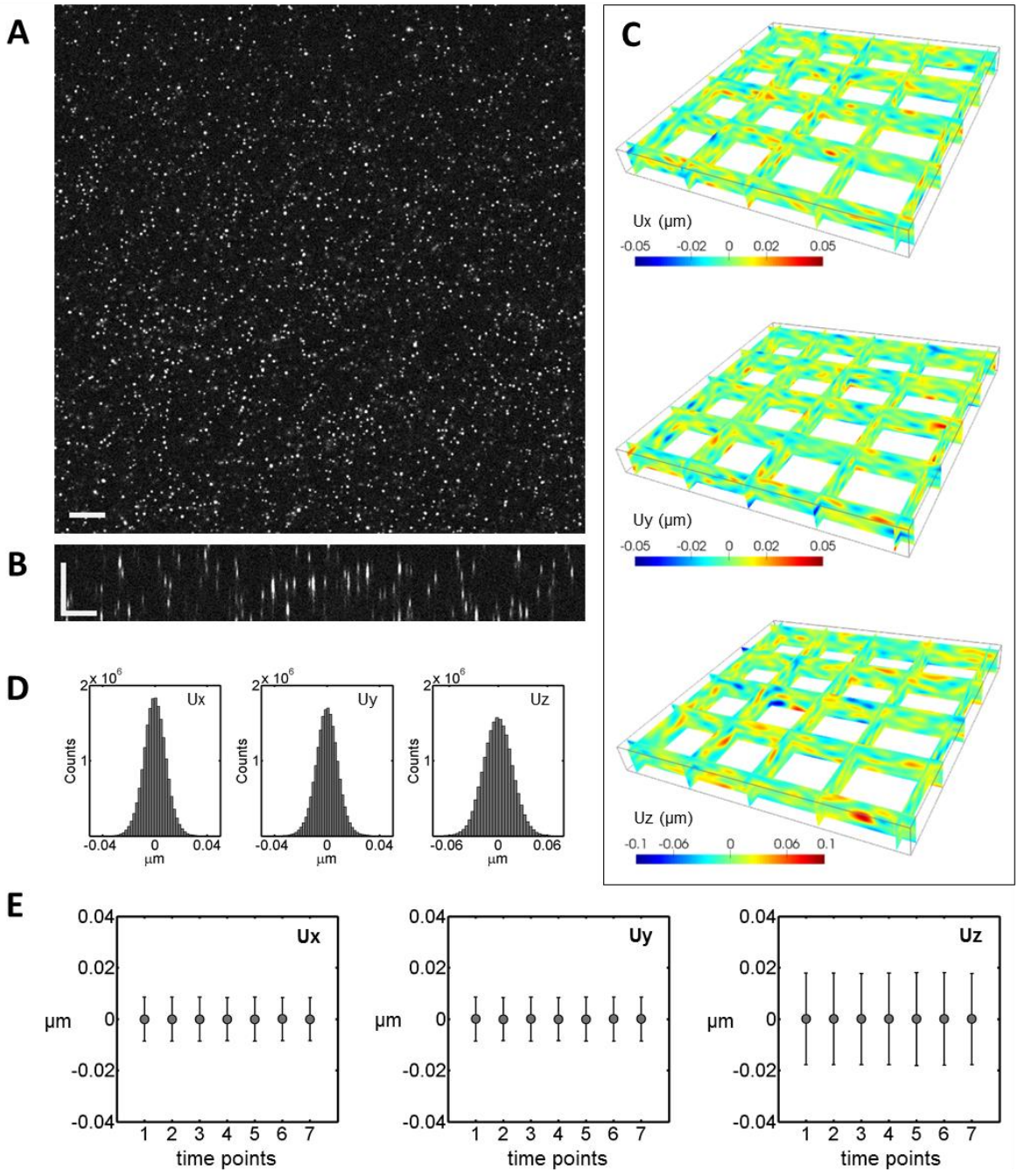

Figure S4. Evaluation of detection limit of the FFD-based displacement calculation method with synthetic data. Sample cross-section (A) and axial-section (B) of simulated hydrogel volume containing fluorescent beads. The scale bar: 15 μm. Axial sections at multiple locations of the simulated volume (bounding box: 220 x 220 x 23 μm^3) showing displacements without the spurious distribution observed in real sham experiments (C), and their corresponding histograms (D). Mean errors (± standard deviation) in the raw (non-corrected) displacements for different time points (E). The obtained small variance in (D) and (E) is caused by the time-varying noise introduced in the simulated images.

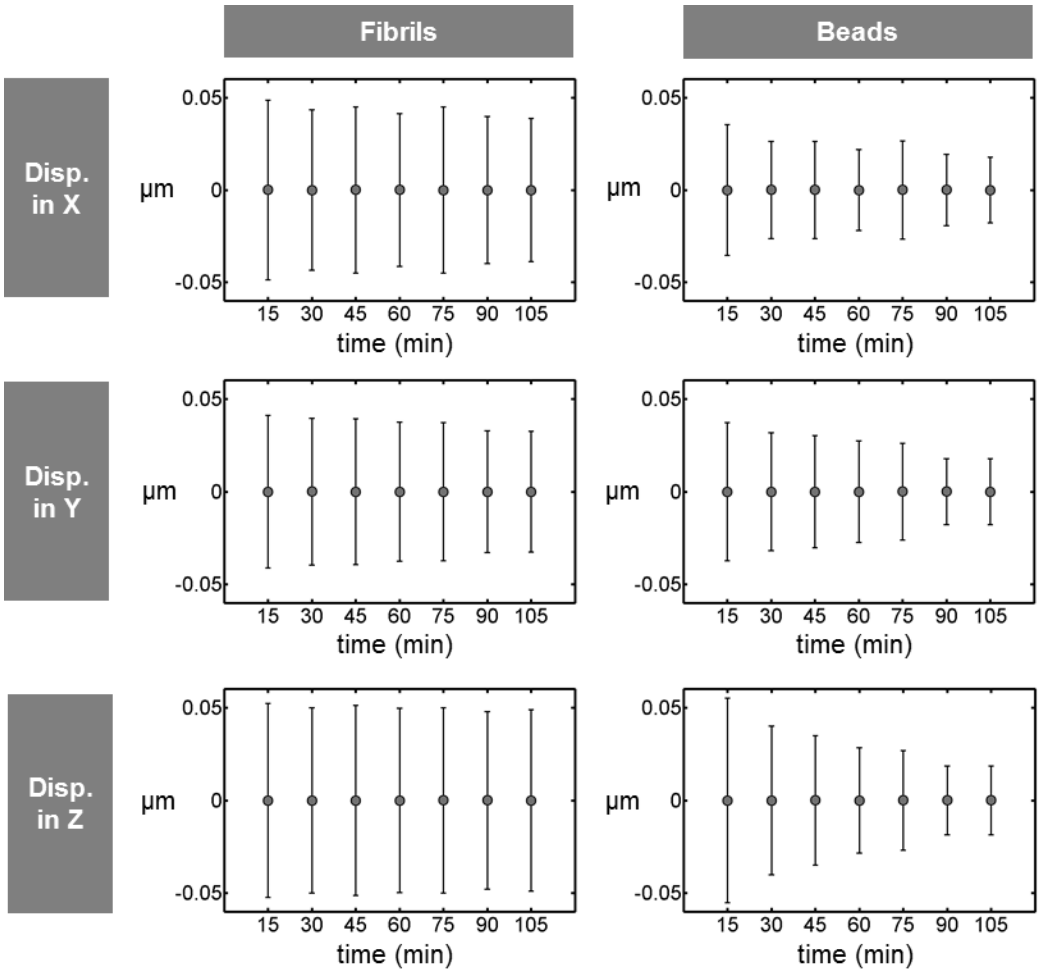

Figure S5. Detection limit of the FFD-based displacement calculation method from sham experiments. Mean errors (± standard deviation) in the X- (top row), Y- (middle row) and Z- (bottom row) components of the displacements computed from fibril- (left column) and bead-based (right column) images after the proposed correction (see main text).

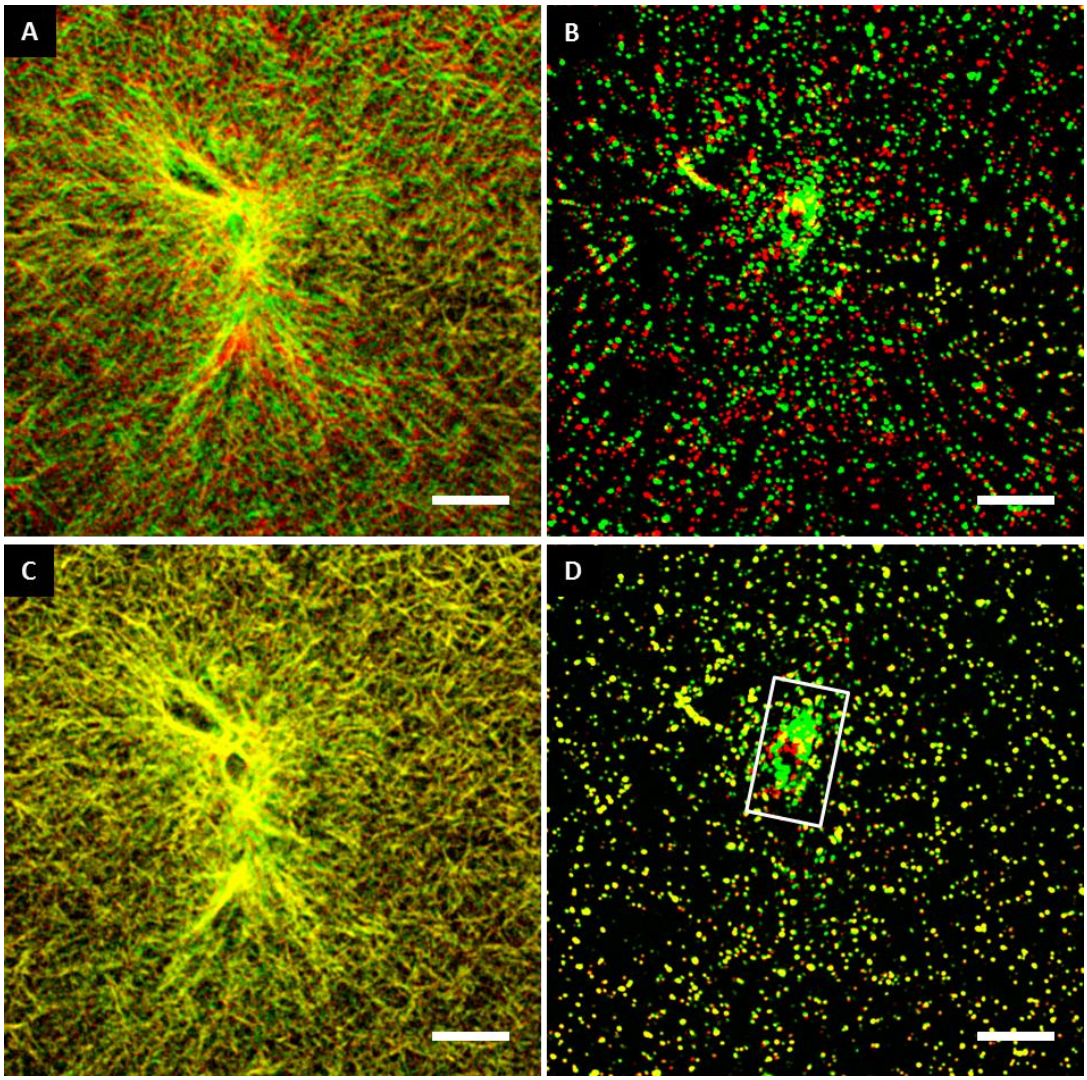

Figure S6. FFD-based image registration of the unstressed and stressed (before addition of cytochalasin B) gel of 4.0 mg/ml collagen concentration. Pseudo-colored cross-sections of the collagen hydrogel showing the fibril- (A) and bead-based (B) images before the registration, and their registered results (C) and (D), respectively, that lead to the recovered displacement field. The fibrils/beads in the unstressed and stressed hydrogel are pseudo-colored in red and green, respectively. Fibrils/beads appear as yellow where both the unstressed and stressed conditions match. The beads engulfed by the cell are ignored during the registration process (D, delineated area) to avoid artifacts in the recovered displacements. Scale bars: 25 μm.

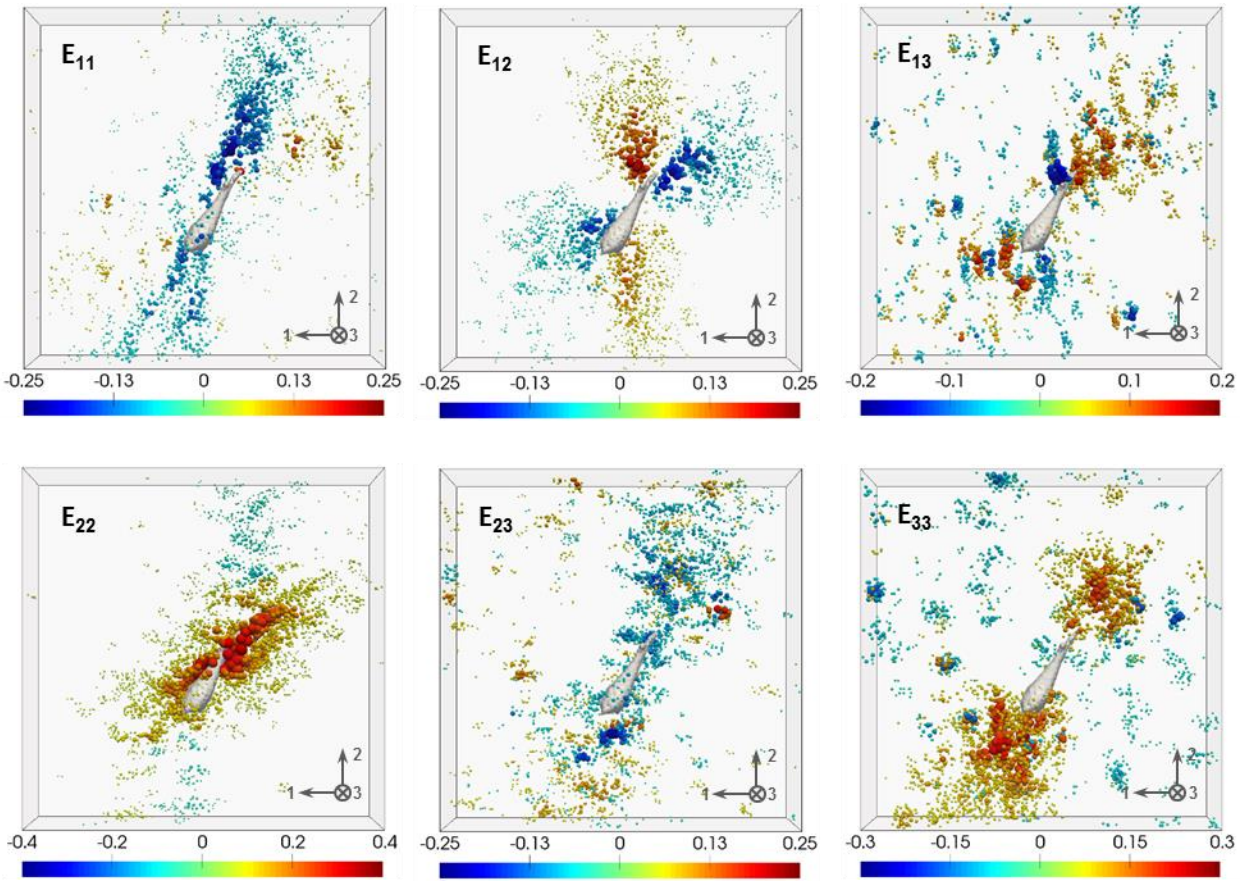

Figure S7. Symmetric Green-Lagrange strain tensor for a sample cell in 4.0 mg/ml collagen depicted in Figure S9B. The maps have been uniformly sampled at random locations to allow the 3D visualization of each component of the tensor.

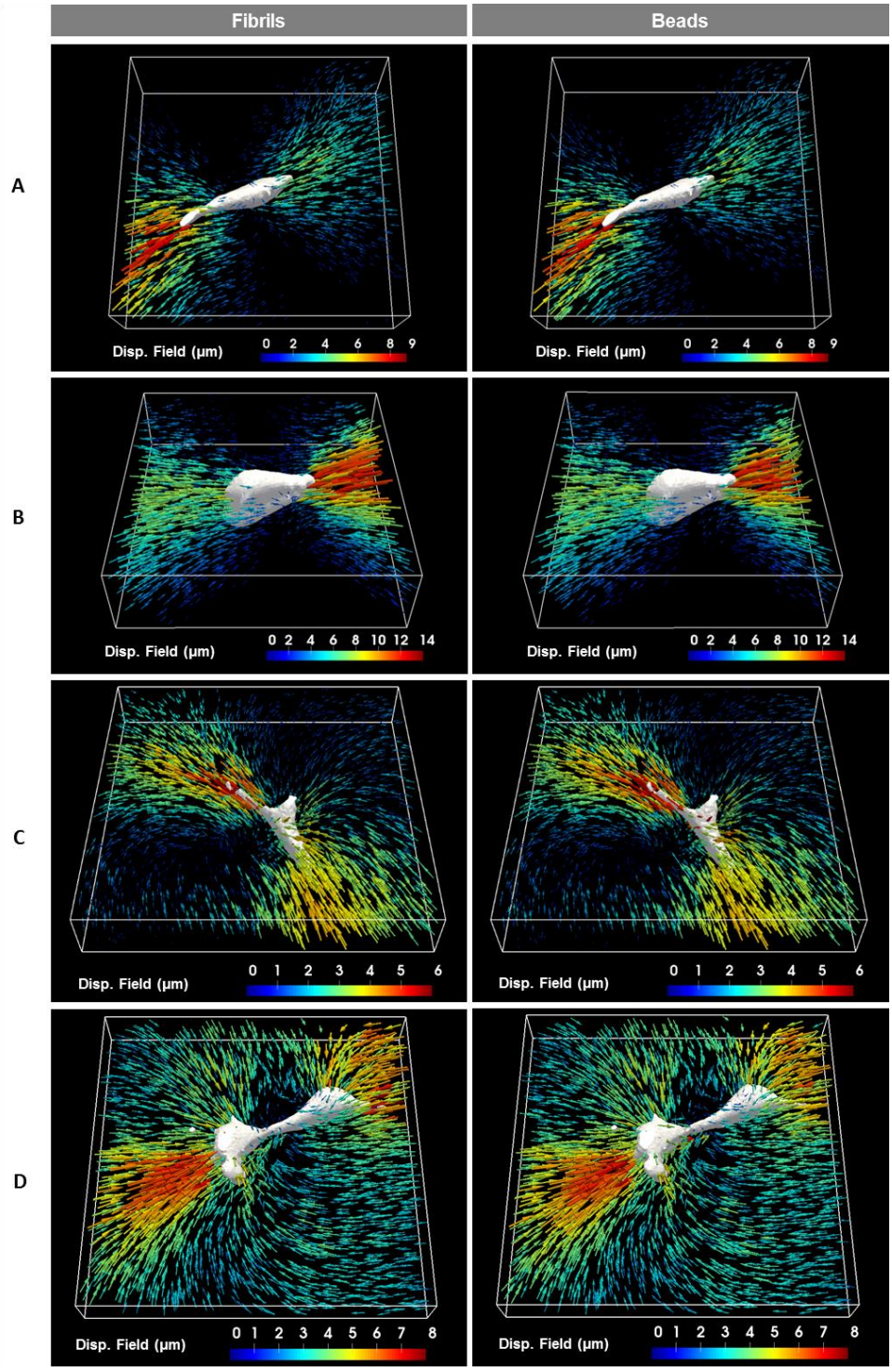

Figure S8. Representative 3D displacements induced by 4 different MRC-5 fibroblasts embedded in 2.4 mg/ml (A, B,C,D) obtained from the registration of fibril-based images (left column) and bead-based images (right column). Bounding box: 170 x 170 x 46 μm^3 (A), 165 x 170 x 48 μm^3 (B), 173 x 172 x 30 μm^3 (C) and 166 x 168 x 22 μm^3 (D).

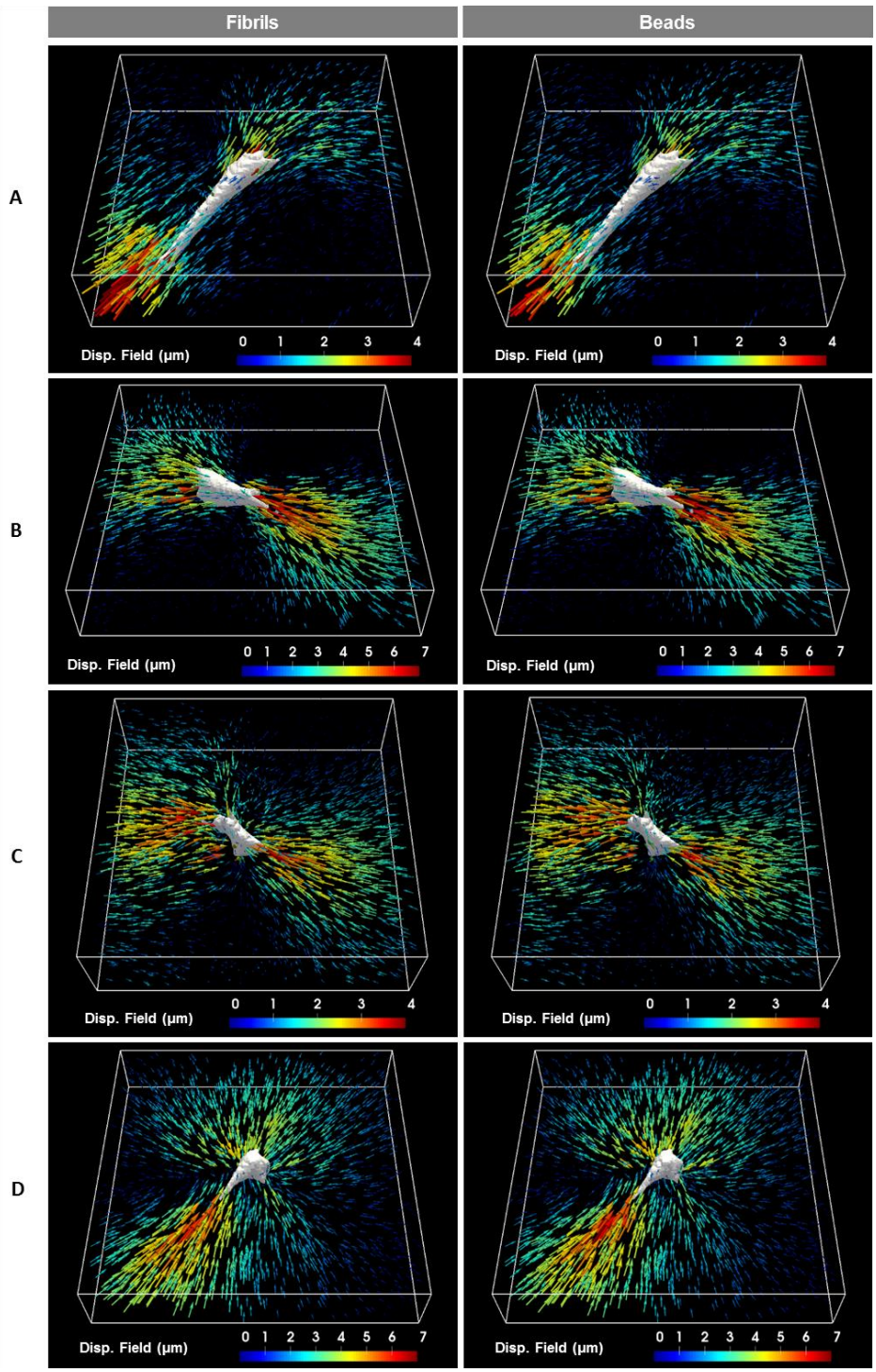

Figure S9. Representative 3D displacements induced by 4 different MRC-5 fibroblasts embedded in 4.0 mg/ml (A, B,C,D) obtained from the registration of fibril-based images (left column) and bead-based images (right column). Bounding box: 172 x 172 x 49 μm^3 (A), 173 x 173 x 37 μm^3 (B), 172 x 172 x 51 μm^3 (C) and 172 x 172 x 34 μm^3 (D).

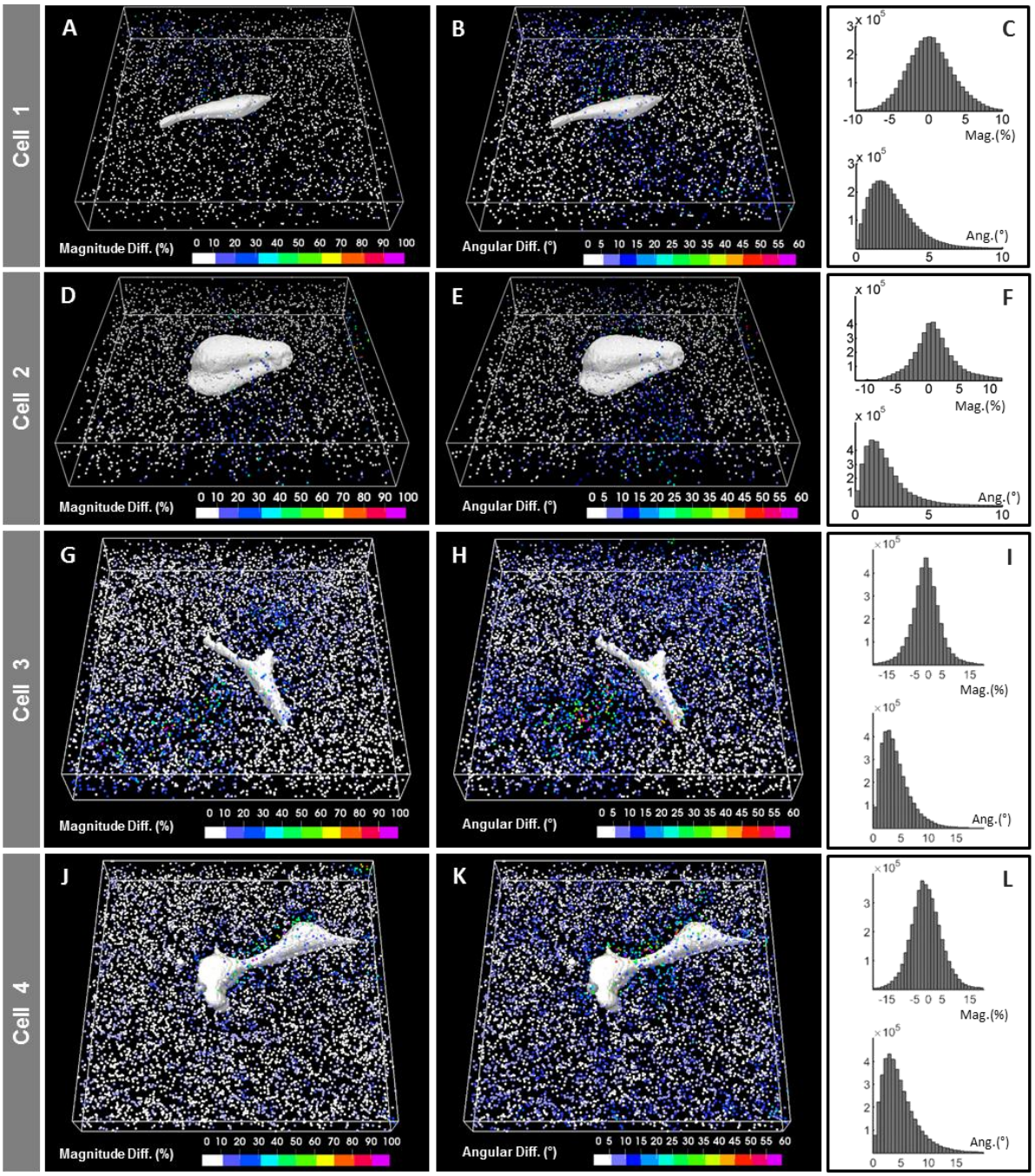

Figure S10. Quantitative comparison between the displacements computed from fibril- and bead-based images for cells in 2.4 mg/ml collagen gels and shown in Figure S8 A (cell 1), S8 B (cell 2), S8 C (cell3) and S8 D (cell4). Map of the relative difference (%) between displacement magnitudes (A,D,G,J) and the angle (degrees) between displacement vector directions (B,E,H,K). Histograms of the differences (C,F,I,L) are computed from those regions exhibiting a displacement magnitude larger than 30% of its peak value.

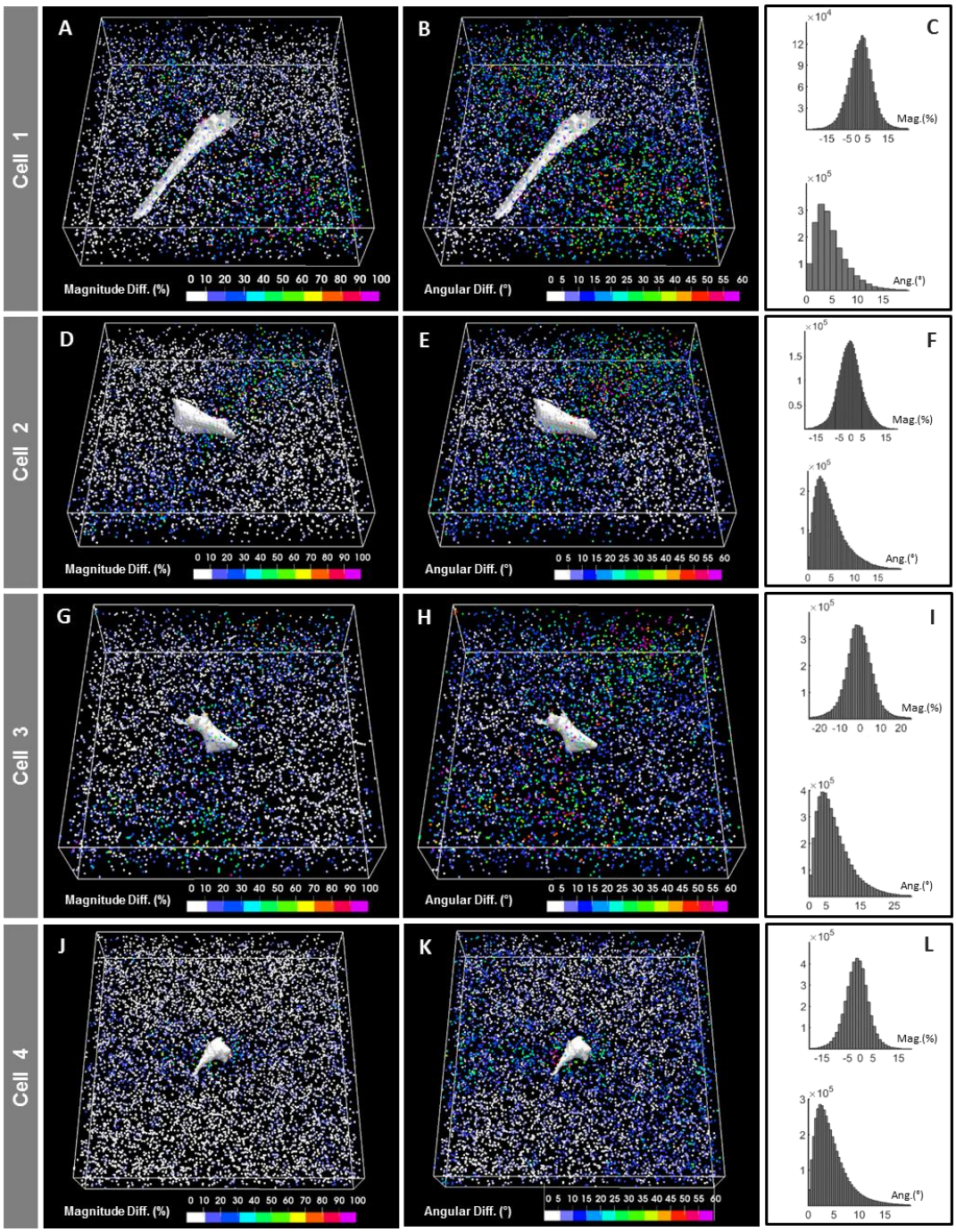

Figure S11. Quantitative comparison between the displacements computed from fibril- and bead-based images for cells in 4.0 mg/ml collagen gels and shown in Figure S9 A (cell 1), S9 B (cell 2), S9 C (cell3) and S9 D (cell4). Map of the relative difference (%) between displacement magnitudes (A,D,G,J) and the angle (degrees) between displacement vector directions (B,E,H,K). Histograms of the differences (C,F,I,L) are computed from those regions exhibiting a displacement magnitude larger than 30% of its peak value.

Supplementary Videos

Supplementary Video 1. Time lapse image series showing the 3D displacements induced by a MRC-5 fibroblast embedded in a 2.4 mg/ml collagen gel during cytochalasin induced force relaxation. Displacement fields were obtained from the registration of fibril-based images (left) and bead-based images (right). Bounding box: 170 x 170 x 21 μm^3.

References

[1] D.L. Kolin, P.W. Wiseman, Advances in image correlation spectroscopy: measuring number densities, aggregation states, and dynamics of fluorescently labeled macromolecules in cells., Cell Biochem. Biophys. 49 (2007) 141–64. doi:10.1007/s12013-007-9000-5.

[2] P.W. Wiseman, Image correlation spectroscopy: Mapping correlations in space, time, and reciprocal space, Methods Enzymol. 518 (2013) 245–267. doi:10.1016/B978-0-12-388422-0.00010-8.

[3] D.L. Kolin, S. Costantino, P.W. Wiseman, Sampling effects, noise, and photobleaching in temporal image correlation spectroscopy., Biophys. J. 90 (2006) 628–39. doi:10.1529/biophysj.105.072322.

[4] B. Hebert, S. Costantino, P.W. Wiseman, Spatiotemporal image correlation spectroscopy (STICS) theory, verification, and application to protein velocity mapping in living CHO cells., Biophys. J. 88 (2005) 3601–3614. doi:10.1529/biophysj.104.054874.